CCT-WG5 on Radiation Thermometry

Uncertainty Budgets for Calibration of Radiation Thermometers below the Silver Point

Joachim Fischer (PTB), Peter Saunders (MSL), Mohamed Sadli (LNE-INM/CNAM), Mauro Battuello (INRiM), Chul Woung Park (KRISS), Yuan Zundong (NIM), Howard Yoon (NIST), Wang Li (NMC/SPRING), Eric van der Ham (NMi/VSL), Fumihiro Sakuma (NMIJ/AIST), Yoshiro Yamada (NMIJ/AIST), Mark Ballico (NML), Graham Machin (NPL), Nigel Fox (NPL), Jörg Hollandt (PTB), Mikhail Matveyev (VNIIM), Pieter Bloembergen, Sevilay Ugur

Contents

1. SCOPE **2**

2. CALIBRATION EQUATIONS **3**

3. PROPAGATION OF UNCERTAINTY **4**

4. UNCERTAINTY COMPONENTS **7**

4.1 UNCERTAINTIES ASSOCIATED WITH THE BLACKBODY 7
4.1.1 Calibration Temperature 7
4.1.2 Impurities 8
4.1.3 Plateau Identification 9
4.1.4 Blackbody Emissivity, Isothermal 10
4.1.4.1 Fixed-Point Blackbodies 10
4.1.4.2 Variable-Temperature Blackbodies 11
4.1.4.3 Cavity Emissivity Uncertainty Components 11
4.1.5 Blackbody Emissivity, Non-Isothermal 12
4.1.5.1 Effective Temperature Approach for Non-Isothermal Cavities 13
4.1.6 Reflected Ambient Radiation 13
4.1.7 Heat Loss Effects 15
4.1.7.1 Radiant Heat Exchange 15
4.1.7.2 Convection Heat Loss 16
4.1.8 Cavity Bottom Uniformity 17
4.1.9 Ambient Conditions 18

4.2 UNCERTAINTIES ASSOCIATED WITH THE RADIATION THERMOMETER 19
4.2.1 Size-of-Source Effect 19
4.2.1.1 Near Infrared 19
4.2.1.2 Mid-Infrared and Thermal Infrared 19
4.2.2 Non-linearity 20
4.2.3 Effect of Instrument Temperature 21
4.2.3.1 Reference Temperature 22
4.2.3.2 Ambient Temperature 22
4.2.4 Atmospheric Absorption 24
4.2.5 Gain Ratios 24
4.2.6 Noise 25

4.3 INTERPOLATION ERROR 25

4.4 DRIFT 27

5. PROPAGATION OF UNCERTAINTY CALCULATIONS **29**

5.1 INTERPOLATION 29

5.2 LEAST-SQUARES FITTING 30

5.3 INCLUSION OF IN-USE UNCERTAINTY COMPONENTS 30
5.3.1 Non-Linearity Components 31
5.3.2 Other Components 31

5.4 UNCERTAINTY PLOTS 31

APPENDIX – INCLUSION OF THE IN-USE NON-LINEARITY UNCERTAINTY COMPONENT **37**

REFERENCES **39**

1. Scope

Recently, the CCT WG5 prepared a working document cataloguing each uncertainty component in the realisation of ITS-90 by radiation thermometry above the silver point [1]. Radiation thermometry is also widely used below the silver point, particularly in many industrial applications. While the ITS-90 technique is applicable in this temperature range, difficulties associated with direct measurement of the relative spectral responsivity at the longer wavelengths required preclude its use. Instead, because of the availability of multiple fixed points and contact thermometers that can measure the temperature of blackbodies according to ITS-90, simpler methods are used to calibrate radiation thermometers below the silver point. These methods involve determining (or approximating) the relationship between thermometer signal, $S(T)$, and blackbody temperature, T:

$$S(T) = \int_0^\infty R(\lambda) L_\mathrm{b}(\lambda, T) d\lambda \,, \tag{1}$$

without measuring the thermometer's spectral responsivity, $R(\lambda)$.

This document presents an analysis of all the uncertainty components contributing to the approximation of ITS-90 below the silver point. As for [1], this is a joint effort of the CCT WG5 and summarises the knowledge and experience of all experts in this field. This document is limited in scope to those thermometers whose signal is proportional to the detector photocurrent. This precludes thermometers that read directly in temperature. Specific examples are presented for three types of thermometer with typical operating wavelengths and bandwidths, and associated temperature ranges: near-infrared thermometers working near 0.9 μm and measuring temperatures from 420 °C to 1085 °C or working near 1.6 μm and measuring temperatures from 150 °C to 962 °C; mid-infrared thermometers with wavelengths near 3.9 μm and measuring temperatures from 20 °C to 962 °C or near 4.6 μm and measuring temperatures from –30 °C to 500 °C; and thermal infrared thermometers with wavelengths from 8 μm to 14 μm and measuring temperatures from –40 °C to 500 °C (sometimes referred to as 10 μm thermometers). Because the wavelengths involved are relatively long, the analysis is performed using the full Planck's law. On the occasions where the Wien approximation is used (for purposes of insight), this is explicitly stated. The effects of thermometer bandwidth are also fully included in the uncertainty analysis.

For near-infrared thermometers measuring temperature above the indium point, the instruments and their characterisation techniques are very similar to thermometers working in the visible and are relatively well established; much of what is described in [1] is of relevance. However, for mid- and thermal infrared thermometers, especially below the indium point, the technique is still premature. It should be noted that for these thermometers this document is, therefore, a summary of techniques established so far, which await further development in future.

In the interests of promoting harmonisation and ensuring consistency with the ISO *Guide to the Expression of Uncertainty in Measurement* [2], we have endeavoured to adhere to the following principles:

- Unless otherwise stated, all uncertainties are expressed as standard uncertainties.
- All uncertainty terms are associated with a physical cause. This ensures that each of the identified sources of uncertainty has a mathematical model allowing estimation and propagation of uncertainty.
- Corrections are applied where bias (systematic error) is known to exist, including in most cases where the correction is less than the uncertainty. This is done to maximise the information retained in reported measurement results and to prevent accumulation of bias effects.
- Where Type A assessments are employed, all of the sources of uncertainty should be identified and the measurements should draw samples from the whole of the distribution associated with each source. This practice prevents both "double counting" and underestimates of uncertainty. This requirement may preclude the use of non-specific uncertainty terms such as "repeatability" and "reproducibility".

2. Calibration Equations

Below the silver point, radiation thermometers can be calibrated using the multi-point method suggested by Sakuma and Hattori [3]. Using this method, the thermometer's signal as a function of temperature, equation (1), is approximated by a calibration equation containing a number of adjustable parameters. This technique allows the thermometer to be calibrated without any knowledge of its spectral responsivity.

It has been shown that calibration equations for radiation thermometers have the general form [4]

$$S(T) = \frac{C}{\exp\left(\frac{c_2}{\lambda_x T}\right) - 1}, \tag{2}$$

where $c_2 = 0.014388$ m.K, C is a proportionality constant, and λ_x is a temperature-dependent effective wavelength called the extended effective wavelength [4]. For most radiation thermometers, the extended effective wavelength is well approximated by a linear function of inverse temperature:

$$\lambda_x = A + \frac{B}{T}, \tag{3}$$

where A and B are constants, giving a specific form to the calibration equation (2):

$$S(T) = \frac{C}{\exp\left(\frac{c_2}{AT + B}\right) - 1}. \tag{4}$$

This is the Planck version of the well-known Sakuma–Hattori equation [3], which is identical to equation (4) except it does not contain the –1 in the denominator. Other forms of equation (2) are sometimes used as calibration equations [4–6], but empirical evidence suggests that equation (4) provides the best comprise between accuracy and number of adjustable parameters. It also has the useful feature that it is easily inverted to give T as an analytic function of S. The uncertainty budgets presented in this paper will be calculated with explicit reference to equation (4) (and in a few cases its Wien version). However, the results for other reasonable three-parameter equations do not differ significantly.

The parameters A, B, and C are determined from pairs of temperature–signal calibration points, (T_i, S_i), where $i = 1, 2, \ldots, N$, with $N \geq 3$. When $N = 3$, equation (4) is known as an interpolation equation, and A, B, and C are solved so that the equation passes exactly through each of the 3 calibration points. When $N > 3$, the parameters A, B, and C are determined from a least-squares fit to the calibration points. The uncertainty in temperatures determined using equation (4) arises from uncertainties in the calibration points (T_i, S_i), from the quality of the match of the calibration equation to the actual signal response of the thermometer (referred to as interpolation error; this name will be used for both interpolation and least-squares fitting), and from uncertainties associated with the measurement of the signal at the unknown temperature. This paper catalogues each uncertainty component and evaluates how each component propagates into the unknown temperature. The interpolation error will be treated as a constant temperature uncertainty component that applies to all temperatures in the calibration range.

3. Propagation of Uncertainty

In this paper we consider two calibration schemes for radiation thermometers below the silver point. One of these uses fixed-point blackbodies (FPBB scheme) to obtain the calibration points (T_i, S_i) and the other uses variable-temperature blackbodies with a separate reference thermometer (VTBB scheme). (In practice a calibration may consist of a combination of these two schemes.) From an uncertainty analysis perspective, the only difference between these two schemes is the nature and number of the individual uncertainty components that contribute to the total uncertainty. These are listed in Table 1 for the two schemes, where a shaded box indicates that the component must be included. The table is split into those components related to the blackbody and those related to the radiation thermometer under calibration. Each component is treated as *either* an uncertainty in the temperature of the blackbody, $u_x(T_i)$, *or* an uncertainty in the signal measured by the radiation thermometer, $u_x(S_i)$. Note that the subscript i refers to the calibration point and the subscript x to the uncertainty component for that point. As a matter of mathematical convenience, some of the components related to the blackbody are treated as signal uncertainties and some of those related to the thermometer are treated as temperature uncertainties. In addition to the uncertainties in the calibration points, there is also an interpolation error component, which is a constant across the calibration range, a component due to drift, which is a function of the source temperature when the thermometer is used at some time after its calibration, and components related to measurement of the signal at the unknown temperature.

For the uncertainties associated with each calibration point, the quadrature sum of all the temperature components for that point is represented by $u(T_i)$ and the quadrature sum of all the signal uncertainties by $u(S_i)$. These can be propagated through equation (4) directly to the unknown temperature, without requiring the intermediate step of propagation to the A, B, and C parameters, which would necessarily involve consideration of correlations [7].

The ISO *Guide to the Expression of Uncertainty in Measurement* [2] gives the formula for combining uncertainties, which applied to equation (4), in the absence of correlations, is

$$u_{\mathrm{c}}^2(T) = \left[\sum_{i=1}^{N} \left(\frac{\partial S(T)}{\partial T_i} u(T_i) \right)^2 + \sum_{i=1}^{N} \left(\frac{\partial S(T)}{\partial S_i} u(S_i) \right)^2 \right] \left(\frac{\partial S(T)}{\partial T} \right)^{-2} . \tag{5}$$

The sensitivity coefficients $\partial S(T)/\partial T_i$ and $\partial S(T)/\partial S_i$, which differ for interpolation ($N = 3$) and least-squares fitting ($N > 3$), will be given in Sections 5.1 and 5.2, respectively. The total uncertainty is the quadrature sum of $u_{\mathrm{c}}(T)$, the uncertainty due to interpolation error, u_{18}, the uncertainty due to drift, $u_{19}(T)$, and the uncertainties occurring at the unknown temperature, $u_{20}(T)$:

$$u_{\mathrm{total}}^2(T) = u_{\mathrm{c}}^2(T) + u_{18}^2 + u_{19}^2(T) + u_{20}^2(T) . \tag{6}$$

The uncertainty component $u_{20}(T)$ is a catch-all for the many contributions that occur when the thermometer is used, which includes many of the same u_1 to u_{17} components contributing to the calibration, but evaluated at the unknown temperature, T. Most of these must be treated separately according to the nature of the source and conditions during measurement. However, for some of the contributions there will exist strong correlations between the components during calibration and use, which will lead to partial or total cancellation of that term. The most obvious of these is non-linearity, which is almost entirely a property of the thermometer and is not influenced by external conditions. To avoid dealing with correlation coefficients for these terms, they will be treated explicitly as part of the calibration and thus will not need to be included in the $u_{20}(T)$ component.

For interpolation, the nature of the sensitivity coefficients allows conversion between uncertainty components in signal and uncertainty components in temperature at any of the calibration points through the relationship

$$u_x(T_i) = \frac{\lambda_{T_i} T_i^2 \left[1 - \exp\left(-c_2 / \lambda_{T_i} T_i \right) \right]}{c_2} \frac{u_x(S_i)}{S_i} . \tag{7}$$

In the Wien approximation, this reduces to

$$u_x(T_i) = \frac{\lambda_{T_i} T_i^2}{c_2} \frac{u_x(S_i)}{S_i} . \tag{8}$$

The extra factor in square brackets in equation (7) is equal to about 0.85 at 500 °C for an 8 μm to 14 μm thermometer and about 0.95 at the silver point for a 3.9 μm thermometer, so for these thermometers there is a significant difference between equations (7) and (8). However, at 0.9 μm and 1.6 μm the difference is negligible even at the silver point.

Table 1. Uncertainty components for the two calibration schemes. The shaded boxes indicate the uncertainty components used under the respective schemes.

	Description	Quantity	FPBB Scheme	VTBB Scheme
Blackbody	Calibration temperature	$u_1(T_i)$		
	Impurities	$u_2(T_i)$		
	Plateau identification	$u_3(T_i)$		
	Blackbody emissivity, isothermal	$\frac{u_4(S_i)}{S_i}$		
	Blackbody emissivity, non-isothermal	$u_5(T_i)$		
	Reflected ambient radiation	$u_6(T_i)$		
	Cavity bottom heat exchange	$u_7(T_i)$		
	Convection	$u_8(T_i)$		
	Cavity bottom uniformity	$u_9(T_i)$		
	Ambient conditions	$u_{10}(T_i)$		
Radiation Thermometer	Size-of-source effect	$\frac{u_{11}(S_i)}{S_i}$		
	Non-linearity	$\frac{u_{12}(S_i)}{S_i}$		
	Reference temperature	$u_{13}(T_i)$		
	Ambient temperature	$\frac{u_{14}(S_i)}{S_i}$		
	Atmospheric absorption	$\frac{u_{15}(S_i)}{S_i}$		
	Gain ratios	$\frac{u_{16}(S_i)}{S_i}$		
	Noise	$u_{17}(T_i)$		
Calibration Equation	Interpolation error	u_{18}		
Use	Drift	$u_{19}(T)$		
	Unknown temperature	$u_{20}(T)$		

Table 2. Typical values of the A and B parameters of the Sakuma–Hattori equation, the mean wavelength, λ_0, and values of the extended effective wavelength and limiting effective wavelength over typical temperature ranges as calculated by equations (3) and (11), respectively.

Spectral Responsivity	A / μm	B / μm.K	λ_0 / μm	Bandwidth / μm	Temperature Range / °C	λ_x Range / μm	λ_T Range / μm
0.9 μm	0.896	5.91	0.899	0.083	420 to 1085	0.905 to 0.900	0.914 to 0.905
1.6 μm	1.58	5.16	1.590	0.105	150 to 962	1.592 to 1.584	1.604 to 1.588
3.9 μm	3.90	1.80	3.904	0.165	20 to 962	3.906 to 3.901	3.912 to 3.903
8 μm to 14 μm	9.61	151	11.00	6.00	–40 to 500	10.26 to 9.81	10.95 to 10.00

For least-squares fitting, equation (7) is not strictly valid since the correct relationship involves the signal residuals, $S_i - S(T_i)$, which are not generally zero (see Section 5.2).

Similar expressions to equations (7) and (8) also hold for the uncertainties at the unknown temperature, with T_i replaced by T and S_i replaced by S.

In equations (7) and (8), λ_{T_i} is the limiting effective wavelength, λ_T, evaluated at the calibration temperature, T_i. The relationship between the limiting effective wavelength and the extended effective wavelength, λ_x, is given by

$$\frac{1}{\lambda_T\left[1-\exp\left(-c_2/\lambda_T T\right)\right]} = \frac{1}{\lambda_x\left[1-\exp\left(-c_2/\lambda_x T\right)\right]}\left(1+\frac{T}{\lambda_x}\frac{d\lambda_x}{dT}\right). \tag{9}$$

The ratio of the two factors in square brackets is very close to 1, so the simpler Wien version of equation (9) may be used for all practical values of λ_x:

$$\frac{1}{\lambda_T} = \frac{1}{\lambda_x}\left(1+\frac{T}{\lambda_x}\frac{d\lambda_x}{dT}\right). \tag{10}$$

Thus, with λ_x given by equation (3), λ_T is

$$\lambda_T = A\left(1+\frac{B}{AT}\right)^2. \tag{11}$$

If $B/AT \ll 1$, then equation (11) becomes $\lambda_T = A + 2B/T$. Approximate values for A and B are given in Table 2 for typical spectral responsivities centred on 0.9 μm, 1.6 μm and 3.9 μm, and for a rectangular 8 μm to 14 μm spectral responsivity. Also shown in Table 2 are the mean wavelength, λ_0, (this is equal to the centre wavelength for symmetrical spectral responsivities), the bandwidth (full width at half maximum), and the variations in λ_x and λ_T for typical temperature ranges that each thermometer is used over. The effective wavelengths vary significantly with temperature for the 8 μm to 14 μm thermometer, and in this case they do not overlap the centre wavelength in the temperature range considered.

4. Uncertainty Components

This section discusses each of the uncertainty components listed in Table 1. For each component, numerical uncertainties are given under the categories of "normal" and "best". Normal uncertainties refer to those easily obtained at present in national metrology institutes, and best uncertainties are those obtained with considerable effort by a small number of leading workers in the field. For mid-infrared thermometers, normal uncertainties usually refer to systems with thermal detectors with operating wavelengths close to 3.9 μm, and best uncertainties can be achieved with thermometers equipped with quantum detectors operating close to 4.6 μm. All uncertainties quoted in this paper are standard uncertainties ($k = 1$).

The uncertainties given in Sections 4.1 and 4.2 below are those associated with the measurements at the calibration points, i.e. with the determination or specification (for FPBBs) of the temperature of a blackbody on the one hand and the measurement of the thermometer signal at the calibration temperatures on the other. The temperature uncertainties are listed as absolute quantities and the signal uncertainties as relative quantities. In the cases where relative signal uncertainties are given, equivalent temperature uncertainties (as determined by equation (7)) are also provided to enable direct comparison of the different components. Section 4.3 discusses the uncertainty due to interpolation error, and drift is discussed in Section 4.4. All the components are propagated in Section 5 to give total uncertainty as a function of source temperature.

4.1 Uncertainties Associated with the Blackbody

4.1.1 Calibration Temperature

This contribution only applies to the VTBB scheme. In the low-temperature range the temperature of variable-temperature blackbodies is, for best accuracy, measured according to the ITS-90 via standard platinum resistance thermometers (SPRTs) positioned near the bottom of the cavity and in good thermal contact with the heat transfer agent. For normal accuracy the temperature measurement may be performed with a Pt100, a thermocouple, or any other secondary thermometer. The overall uncertainty of the temperature measurement stems from three groups of uncertainty contributions: the uncertainty of the calibration of the reference thermometer, the stability of the calibrated thermometer, and the uncertainty of the temperature measurement carried out by the user.

Table 3. Standard uncertainties in the calibration temperature measurement of a variable-temperature blackbody.

Description	Quantity	Probability distribution	Value / mK					
			–30 °C		–10 °C		0 °C	
			normal	best	normal	best	normal	best
Calibration temperature	$u_1(T_i)$	normal	6	0.8	6	0.8	6	0.8

Description	Quantity	Probability distribution	Value / mK					
			23 °C		23 °C to 50 °C		>50 °C to 150 °C	
			normal	best	normal	best	normal	best
Calibration temperature	$u_1(T_i)$	normal	6	0.9	6	0.9	12	1.2

Description	Quantity	Probability distribution	Value / mK					
			>150 °C to 270 °C		>270 °C to 500 °C		>500 °C to 960 °C	
			normal	best	normal	best	normal	best
Calibration temperature	$u_1(T_i)$	normal	18	1.3	18	2	100	3

The uncertainty budget of the calibration of SPRTs according to the ITS-90 is discussed in detail in the CCT-documents CCT/2000-16 [8], CCT/2000-17 [9], and CCT/01-02 [10] and the literature cited therein. The stability of the calibrated SPRT may significantly contribute to the uncertainty of the temperature measurement by the user. Its influence, however, will strongly depend on the individual design and handling of the SPRT. Reliable numbers can be deduced from the regular recalibration of an individual SPRT. For SPRTs for which data from only one calibration exists, reasonable assumptions on their stability can be made from propagating their repeatability at the triple point of water during calibration to higher temperatures and longer time periods. Additionally, the effect of possible oxidation and reduction of the platinum sensor above 0 °C and, above the freezing point of zinc, the drift of the SPRT resistance with time due to the ageing of the platinum wire have to be included [10].

Finally, the uncertainty of the temperature measurement by the user can be estimated by the uncertainty of the bridge measurement. The resulting overall uncertainty of the temperature measurement for variable-temperature blackbodies is given in Table 3. For best accuracy the uncertainties of standard platinum resistance thermometers are estimated in accordance with CCT/01-02 [10]. For normal accuracy, in the temperature range from –50 °C to 500 °C a wire-wound Pt100 calibrated by comparison to SPRTs in a stirred liquid bath is assumed. In the temperature range above 500 °C the uncertainty of noble metal thermocouples (Type S and Type R) is given.

4.1.2 Impurities

Impurities affect only the FPBB scheme. There are four possible sources of impurity. The first is the impurity of the metal material. The second arises from casting the metal in the crucible. The third source is the impurity of the crucible. Purification after machining of carbon is a prerequisite to its application as a crucible material. The last source is the impurity that comes about while using the crucible.

Metals of five nine (5N) purity and six nine (6N) purity are commercially available from the manufacturers. There are no definite indications of the effects on the fixed-point temperature differences of using purer samples than this, as the results are dependent on the nature and the distribution of the impurities inside the sample. The effect of impurities on the Zn point is discussed in [11]. A detailed experimental investigation of the effect of impurities on the Al point is reported in [12] and experimental investigations for the Ag and Cu points can be found in [13–15]. Differences of less than 10 mK have been found between 5N and 6N Ag samples. A detailed analysis with references on the influence of impurities can also be found in [10, 16, 17].

The oxidation effect is more important in radiation thermometry than in contact thermometry because open cells are used in the former. Silver has been extensively investigated; according to the phase diagram, 0.3 % by weight of oxygen will cause a decrease of about 21 °C in the freezing temperature [18]. However, such large oxidation effects have not been reported in practice. NMIJ's experience with silver-point blackbodies is that they agree within 0.1 °C after long-term use [19]. In radiation thermometry, oxidation of copper and silver is prevented by the presence of carbon at high temperature but it is not so effective for aluminium. Aluminium is often found to oxidise during use. Fortunately, oxides with aluminium do not dissolve in liquid aluminium [18]. The effect of oxidation is not clear for zinc and other fixed-point metals with even lower transition temperatures. Indium is easily oxidised at its surface and oxygen will penetrate inside the metal over time. Gallium also forms an oxidised surface layer. More information is necessary on the effect of metal oxidation.

According to reference [17] there are two methods for estimating the uncertainty of fixed-point temperatures due to the effect of impurities. The first one is the sum of the individual estimates (SIE). This method requires knowledge of each impurity content and of the corresponding liquidus slopes and distribution coefficients; presumably it can be applied to materials with purities better than 99.999%. The second method is the overall maximum estimate (OME). It has to be applied here since the concentrations of the impurities and their influence on the fixed-point temperature are not known as accurately as needed for the SIE method to be applicable.

Assuming that impurities with a distribution coefficient, k, larger than 2 can be disregarded restricts the extremes of the deviation of the liquidus temperature from that of the pure system to

$$\Delta T_{\mathrm{OME,\,extr}} = \pm c_{l1} / A \,. \tag{12}$$

In equation (12), c_{l1} is the overall impurity concentration, expressed in mole fraction, at the liquidus point and A is the first cryoscopic constant. Equation (12) can be derived from the relationship between liquidus slope and distribution coefficient, k, in the ideal-solutions approximation. The global treatment of the influence of the impurities, expressed by equation (12), precludes applying a correction as in the case of the SIE. However, taking the probability distribution function related to k as being rectangular with limits of $k = 0$ and $k = 2$ yields the following estimate for the standard uncertainty arising from the impurities in the sample:

Table 4. Standard uncertainties of fixed-point temperatures due to impurities from equation (13) with $c_{l1} = 0.000\ 01$ for normal accuracy and $c_{l1} = 0.000\ 001$ for best accuracy.

Description	Quantity	Probability distribution	Fixed point	Value / mK	
				normal	best
Fixed-point impurities	$u_2(T_i)$	normal	Hg (–38.8344 °C)	1.1	0.1
Fixed-point impurities	$u_2(T_i)$	normal	Ga (29.7646 °C)	0.75	0.1
Fixed-point impurities	$u_2(T_i)$	normal	In (156.5985 °C)	2.7	0.3
Fixed-point impurities	$u_2(T_i)$	normal	Sn (231.928 °C)	1.7	0.2
Fixed-point impurities	$u_2(T_i)$	normal	Zn (419.527 °C)	3.25	0.3
Fixed-point impurities	$u_2(T_i)$	normal	Al (660.323 °C)	3.9	0.4
Fixed-point impurities	$u_2(T_i)$	normal	Ag (961.78 °C)	6.5	0.7

$$u^2(\Delta T_{\mathrm{OME}}) = \left(\Delta T_{\mathrm{OME,\,extr}}\right)^2 \Big/ 3 = \left(c_{l1}/A\right)^2 \Big/ 3\,. \tag{13}$$

To estimate the effect of the uncertainties in impurity content, based upon the OME method, 5N and 6N purity (in terms of mole fraction) are assumed as normal and best cases, respectively. Substituting the A values from reference [10] into equation (13) yields the uncertainties in the fixed-point temperatures given in Table 4.

4.1.3 Plateau Identification

This contribution only applies to the FPBB scheme. If the freeze plateau is of good quality, the fixed-point temperature can be estimated, for example, as the average between 25% and 75% solid fraction of the freeze plateau. The difference between this average value and the maximum of the freezing curve is treated as the uncertainty in the fixed-point temperature, resulting in uncertainties of 10 mK and 2 mK for the normal and best uncertainty, respectively, for all

Table 5. Standard uncertainties of fixed-point temperatures due to plateau identification.

Description	Quantity	Probability distribution	Fixed point	Value / mK	
				normal	best
Plateau identification	$u_3(T_i)$	normal	Hg (–38.8344 °C)	200	50
Plateau identification	$u_3(T_i)$	normal	Ga (29.7646 °C)	50	10
Plateau identification	$u_3(T_i)$	normal	In (156.5985 °C)	10	2
Plateau identification	$u_3(T_i)$	normal	Sn (231.928 °C)	10	2
Plateau identification	$u_3(T_i)$	normal	Zn (419.527 °C)	10	2
Plateau identification	$u_3(T_i)$	normal	Al (660.323 °C)	10	2
Plateau identification	$u_3(T_i)$	normal	Ag (961.78 °C)	10	2

fixed points except for Ga and Hg (see Table 5). At low temperatures calibration becomes difficult due to significant background radiation.

4.1.4 Blackbody Emissivity, Isothermal

Two separate approaches may be taken to determine the effective emissivity of a blackbody cavity – calculation and measurement.

Calculation is the best way to investigate the effective emissivity of blackbodies. A variety of mathematical models have been developed mainly based on the summation method, the series method, or Monte-Carlo simulations [20]. Commercial ray-tracing software that implements the Monte-Carlo method is now available [21, 22]. This software makes it possible to investigate the emissivity of isothermal blackbodies with a complicated geometry. In principle, the spectral bi-directional reflectance distribution function should be used in this calculation. However, in practice this function is never known sufficiently well, and a diffuse–Lambertian or a simple specular–diffuse approximation is used [23–25].

The spectral emissivities of common materials and coatings used for blackbody cavities have been investigated very carefully in [26]; the results provide a sound basis for the calculation of cavity emissivities.

There are experimental methods that allow independent verification of the blackbody emissivity. One of the methods involves illuminating the bottom of the blackbody cavity with a focused laser at the measurement wavelength of the radiation thermometer, and then collecting the light reflected from the cavity using an integrating sphere. It has been found that the measured values are generally a little higher than the calculated values, indicating that the emissivity estimates for the surfaces are slightly underestimated. This method has an uncertainty of about 0.00003 [27].

Another method involves irradiating the blackbody with a modulated thermal infrared flux, and measuring the modulation of the radiation reflected from the blackbody under test. This method has been used to measure the reflectance with an uncertainty of about 0.0002 [28].

These experimental techniques help to check values of the calculated emissivity, and help with the diagnosis of construction defects, such as a poorly defined blackbody apex cone.

4.1.4.1 Fixed-Point Blackbodies

There are variations in the realisation of fixed points for different temperatures. Usually fixed-point blackbodies have the cylindro-cone shape. The uncertainties in the effective emissivity of the cavity arise from an uncertain knowledge of the wall emissivity, geometrical factors, and machining imperfections.

Typical characteristics of fixed-point blackbodies include:

- Isothermal cavity – temperature non-uniformity can be negligible.
- Shape – in most cases cylindrical with conical, hemispherical or grooved bottom, and with aperture.
- Material – graphite; on occasion Teflon-coated metals.
- Size – diameter: 4 mm to 15 mm; length: 30 mm to 110 mm; aperture diameter: 1 mm to 15 mm.

For example, the effective emissivity of a graphite cylindro-cone blackbody with a large aperture for fixed-point calibrations (length: $L = 105$ mm; aperture diameter: $d = 15$ mm; cone half-angle: $\theta = 60°$) is estimated to be 0.9992 from a Monte-Carlo calculation based on the assumptions of isothermal conditions, perfectly diffuse reflection on the cavity surface, and a value of 0.85 for the emissivity of graphite. This leads, for example, to a standard uncertainty in temperature of 5.4 mK at the Zn point at a wavelength of $\lambda = 4.52$ μm [23].

According to the data measured in [29], the diffusity (i.e., the ratio of diffuse reflectance to the sum of diffuse and specular reflectance) of graphite varies approximately from 0.95 at 2 μm to 0.8 at 19 μm. Neglecting this leads to additional uncertainty in the result of a Monte-Carlo calculation of emissivity. Moreover, the internal surface of a cavity after machining may have a higher specular component of reflection, especially for large angles of incidence. This additional uncertainty is estimated to be 0.00005 at $\lambda = 1.6$ μm, 0.0001 at $\lambda = 3.9$ μm, and 0.00025 at $\lambda = 10$ μm. A flat V-grooved cavity bottom shows better diffusity than a conical bottom.

4.1.4.2 Variable-Temperature Blackbodies

Variable-temperature blackbody radiators are usually used for transferring radiance temperatures to radiation thermometers/secondary blackbody radiators, and for transferring them between calibrated and un-calibrated radiation thermometers, possibly operating at different wavelengths.

Typical variable-temperature blackbody characteristics include:

- Non-isothermal cavity – in many cases the temperature distribution inside the cavity becomes so large that it can no longer be disregarded.
- Shape – in most cases cylindrical with conical, hemispherical or grooved bottom, and with aperture.
- Material – graphite, oxidised inconel or stainless steel, covered with stove black, plastic paint, or other high-emissivity coating.
- Size – diameter: 10 mm to 100 mm; length: 60 mm to 560 mm; aperture diameter: 6 mm to 50 mm.

The uncertainties arise from an uncertain knowledge of the intrinsic emissivity of the cavity wall, geometrical factors and machining imperfections.

4.1.4.3 Cavity Emissivity Uncertainty Components

The following factors all contribute to the uncertainty in the cavity emissivity:

- *Intrinsic emissivity of the cavity wall:* The wall emissivity, ε, is generally between 0.75 and 0.95, depending on the material used. Tabulated values for a given sample of graphite, stainless steel, oxidised inconel, or black surface coating have a spread of about ±0.02. However, during machining, the graphite is polished to some extent and develops specularity, and surfaces of stainless steel, oxidised inconel, and coatings change during operation, so a standard uncertainty of $u(\varepsilon) = 0.025$ is more realistic. This leads to an uncertainty in the cavity emissivity of

$$u(\varepsilon_{\mathrm{bb,\,w}}) \approx \frac{1-\varepsilon_{\mathrm{bb}}}{1-\varepsilon}\,u(\varepsilon)\,. \tag{14}$$

- *Geometrical factors:* The cavity dimensions are not perfectly well known. Uncertainties in the cavity length, L, the aperture diameter, d, and cone angle, θ, lead to the following uncertainties in the cavity emissivity:

$$u(\varepsilon_{\mathrm{bb},\,L}) \approx (1-\varepsilon_{\mathrm{bb}})\,\frac{2u(L)}{L}\,, \tag{15}$$

$$u(\varepsilon_{\mathrm{bb},\,d}) \approx (1-\varepsilon_{\mathrm{bb}})\,\frac{2u(d)}{d}\,, \tag{16}$$

and

$$u(\varepsilon_{\mathrm{bb},\,\theta}) \approx (1-\varepsilon_{\mathrm{bb}})\cot\theta\,u(\theta)\,. \tag{17}$$

It is assumed that for normal uncertainty $u(L)/L = 1$ %, $u(d)/d = 1$%, and $u(\theta) = 2.5°$, and for best uncertainty the values are half these numbers.

- *Machining imperfections:* During construction, about $\Delta t = 0.25$ mm of the tip of the conical cavity is slightly rounded (the surface is locally perpendicular to the cavity axis), with a consequently lower local effective emissivity. The radiation thermometer collects radiation from a small region t of the cavity bottom (usually t is about 2 mm). The rounding of the cavity bottom leads to an uncertainty in the cavity emissivity [30] of

$$u(\varepsilon_{\mathrm{bb,\,mac}}) \approx (1-\varepsilon_{\mathrm{bb}})(\mathrm{cosec}\,\theta - 1)\left(\frac{\Delta t}{t}\right)^2\,. \tag{18}$$

The total uncertainty in the cavity emissivity is the quadrature sum of equations (14) to (18). This uncertainty is treated as a signal uncertainty such that the relative signal uncertainty, $u_3(S_i)/S_i$, is equal to the relative uncertainty in the cavity emissivity. Table 6 summarises the uncertainty components for an isothermal fixed-point or variable-temperature blackbody cavity.

Table 6. Standard uncertainties of the effective cavity emissivity for an isothermal fixed-point or variable-temperature blackbody.

Description	Quantity	Prob. dist.	Value		Equivalent temperature uncertainty / mK							
					20 °C, λ=10 μm		500 °C, λ=3.9 μm		500 °C, λ=1.6 μm		750 °C, λ=0.9 μm	
			normal	best	normal	best	normal	best	normal	best	normal	best
Effective emissivity	ε_{bb}		0.999	0.99997								
Wall emissivity	$u(\varepsilon_{bb,\,w})$	normal	0.0005	0.000015	24	0.7	80	2.4	33	1.0	33	1.0
Cavity length	$u(\varepsilon_{bb,\,L})$	normal	0.00002	0.0000003	1.0	0.01	3.2	0.05	1.3	0.02	1.3	0.02
Aperture diameter	$u(\varepsilon_{bb,\,d})$	normal	0.00002	0.0000003	1.0	0.01	3.2	0.05	1.3	0.02	1.3	0.02
Cone angle	$u(\varepsilon_{\theta})$	normal	0.000025	0.000001	1.2	0.05	4.0	0.2	1.7	0.07	1.7	0.07
Machining imperfect.	$u(\varepsilon_{bb,\,mac})$	normal	0.000002	0.0000001	0.1	0.005	0.3	0.02	0.13	0.007	0.13	0.007
Cavity emissivity	$\frac{u_4(S_i)}{S_i}$	**normal**	**0.00050**	**0.000015**	**24**	**0.7**	**80**	**2.4**	**33**	**1.0**	**33**	**1.0**

4.1.5 Blackbody Emissivity, Non-Isothermal

For variable-temperature blackbodies that cannot be guaranteed to be isothermal, measurements of the temperature distribution along the walls of the cavity must be carried out (e.g. with a standard platinum resistance thermometer sensing the bottom of the cavity and up to three quarters of the cylindrical part of the cavity, or with a high resolution radiation thermometer [31]).

The estimation of the effective emissivity of a non-isothermal blackbody can be performed by calculations based on a modified summation method [20] or a modified Monte-Carlo simulation method [32].

For example [33], the cavity is divided into three sections: the cavity bottom, the cylindrical wall and the front lid with the aperture. Using the experimental data for the temperature distribution of the cylindrical part of the cavity, a third-order polynomial fit is performed to describe the temperature distribution. Since experimental data are only available for three quarters of the cylindrical wall, the data for the missing quarter is extrapolated (worst case approach).

This approach is correct only for small departures from isothermal conditions. In this case, the non-isothermal temperature distribution leads to only a perturbation of the emissivity of the blackbody, and the non-isothermal part is taken as the uncertainty. Otherwise the blackbody would need to be modified so as to align the temperature field along the cavity axis. Assuming the whole cavity except the bottom is cooler by a maximum value of ΔT gives a lower limit to the cavity emissivity (worst case estimate). Treating the error as a rectangular distribution with a mean of zero leads to an uncertainty in the cavity emissivity of

$$u(\varepsilon_{bb,\,T}) \approx \frac{c_2(1-\varepsilon)|\Delta T|}{\sqrt{3}\lambda_{T_i} T_i^2 \left[1-\exp\left(-c_2/\lambda_{T_i} T_i\right)\right]}\,. \tag{19}$$

Table 7. Standard uncertainties in blackbody temperature due to uncertainty in the effective cavity emissivity for a non-isothermal blackbody.

Description	Quantity	Prob. dist.	Value / mK	
			normal	best
Cavity emissivity	$u_5(T_i)$	rectangular	35	2.6

Treating equation (19) as relative signal uncertainty and combining it with equation (7) results in a constant cavity temperature uncertainty at all cavity temperatures and wavelengths. Table 7 gives results for a maximum temperature difference ΔT of 400 mK for normal uncertainty and 90 mK for best uncertainty. It is also assumed that $\varepsilon = 0.85$ for the normal case and $\varepsilon = 0.95$ for best.

4.1.5.1 Effective Temperature Approach for Non-Isothermal Cavities

For a given non-isothermal cavity, the effective emissivity depends on both wavelength and temperature. Therefore, effective emissivities have to be evaluated at every wavelength and every temperature associated with the radiation thermometers to be calibrated. In practice, this can complicate the calibration of radiation thermometers at various wavelengths at low temperatures.

The concept of an effective temperature can simplify the characterisation of non-isothermal cavities [34]. The effective temperature, T_e, of a non-isothermal cavity is defined by the equation,

$$L_0(\lambda, T_0) = \varepsilon_c L_b(\lambda, T_e)\,, \tag{20}$$

where $L_0(\lambda, T_0)$ is the spectral radiance of the cavity at the representative temperature T_0, ε_c is the cavity emissivity of the isothermal cavity, and T_e, is a particular reference temperature chosen to make the effective emissivity of the non-isothermal cavity numerically the same as that of the corresponding isothermal cavity. To a first-order approximation, the effective temperature is dependent neither on the wavelength nor the cavity temperature. Even when the cavity has a substantial temperature gradient, the effective temperature is much less wavelength-dependent than the effective emissivity of the corresponding non-isothermal cavity. For example, for a cavity with $T_0 = 1000$ K and a 100 K (10 %) quadratic temperature gradient towards the aperture, T_e is near 999 K and changes only 0.03 % in the spectral range 0.5 μm to 5 μm.

4.1.6 Reflected Ambient Radiation

When viewing a blackbody, a small part of the radiation thermometer's signal arises from ambient radiation that enters the blackbody cavity's aperture and subsequently emerges after multiple reflections. The aperture can be treated as a diffuse reflector with a reflectance equal to $1 - \varepsilon_{bb}$, where ε_{bb} is the effective emissivity of the cavity. Assuming that the ambient radiation originates from a constant-temperature hemispherical source in front of the aperture, then the reflection error can be calculated from the equation:

$$S_m = \frac{\varepsilon_{bb} S(T_i) + (1-\varepsilon_{bb}) S(T_a)}{\varepsilon_{bb}}\,, \tag{21}$$

where S_m is the measured signal, $S(T_i)$ is the signal at the blackbody temperature, T_i, and $S(T_a)$ is the signal at the ambient temperature, T_a. The ε_{bb} term in the denominator of equation (21) indicates that the signal has been corrected for the blackbody's emissivity, so that for $T_a = 0$ there is zero reflection error.

From equation (21) it is easily seen that the relative signal error due to reflected radiation is

$$\frac{\Delta S(T_i)}{S(T_i)} = \frac{S_m - S(T_i)}{S(T_i)} = \frac{S(T_a)}{S(T_i)} \frac{(1-\varepsilon_{bb})}{\varepsilon_{bb}}\,. \tag{22}$$

For typical values of cavity emissivity and ambient temperature, $\Delta S(T_i)$ is small and the reflection error in terms of temperature, ΔT_{refl}, is, to a good approximation, determined by substituting equation (22) into equation (7):

$$\Delta T_{refl} = \frac{\lambda_{T_i} T_i^2}{c_2} \frac{S(T_a)}{S(T_i)} \left[1 - \exp\left(\frac{-c_2}{\lambda_{T_i} T_i}\right)\right] \frac{(1-\varepsilon_{bb})}{\varepsilon_{bb}}\,. \tag{23}$$

This error is illustrated in Table 8 for a range of blackbody temperatures and an ambient temperature of 20 °C. The error is significant for long wavelengths and low temperatures, and is negligible for 0.9 μm and 1.6 μm thermometers. When the error is significant, the measured signal should be corrected by subtracting an amount according to equation (23). The quantity $S(T_a)$ can be determined by measuring an object representative of the temperature of the surroundings, such as a room temperature cavity, and $S(T_i)$ is approximately the signal from the blackbody at the calibration temperature.

The uncertainty in applying this correction is dominated by the uncertainty in the estimate of the blackbody emissivity, ε_{bb}, as given by the quadrature sum of the values in Tables 6 and 7. Expressed as an equivalent uncertainty in temperature, the uncertainty in the correction for reflected radiation is given by

$$u_{10}(T_i) = \frac{\lambda_{T_i} T_i^2}{c_2} \frac{S(T_a)}{S(T_i)} \left[1 - \exp\left(\frac{-c_2}{\lambda_{T_i} T_i} \right) \right] \frac{u(\varepsilon_{bb})}{\varepsilon_{bb}^2} . \quad (24)$$

This is illustrated in Table 9 with $\varepsilon_{bb} = 0.999$ and $u(\varepsilon_{bb}) = 0.0006$ for normal accuracy, and $\varepsilon_{bb} = 0.99997$ and $u(\varepsilon_{bb}) = 0.0001$ for best accuracy.

Table 8. Error in the radiance temperature of a blackbody due to reflected ambient radiation. It is assumed in all cases that the ambient temperature is T_a = 20 °C. Normal values are for a blackbody emissivity of ε_{bb} = 0.999 and best for ε_{bb} = 0.99997.

Description	Quantity	Value / mK for λ=10 μm									
		–40 °C		–20 °C		50 °C		150 °C		500 °C	
		normal	best	normal	best	normal	best	normal	best	normal	best
Reflected ambient radiation	ΔT_{refl}	133	4.0	99	3.0	49	1.5	29	0.9	16	0.5

Description	Quantity	Value / mK for λ=3.9 μm									
		20 °C		100 °C		200 °C		600 °C		960 °C	
		normal	best	normal	best	normal	best	normal	best	normal	best
Reflected ambient radiation	ΔT_{refl}	23	0.7	2.6	0.08	0.5	0.02	0.05	0.001	0.03	0.0008

Description	Quantity	Value / mK for λ=1.6 μm									
		150 °C		300 °C		500 °C		700 °C		960 °C	
		normal	best	normal	best	normal	best	normal	best	normal	best
Reflected ambient radiation	ΔT_{refl}	0.002	5×10^{-5}	7×10^{-6}	4×10^{-7}	4×10^{-7}	1×10^{-8}	5×10^{-8}	2×10^{-9}	1×10^{-8}	4×10^{-10}

Description	Quantity	Value / mK for λ=0.9 μm									
		400 °C		600 °C		750 °C		960 °C		1085 °C	
		normal	best	normal	best	normal	best	normal	best	normal	best
Reflected ambient radiation	ΔT_{refl}	1×10^{-12}	4×10^{-14}	9×10^{-15}	3×10^{-16}	8×10^{-16}	2×10^{-17}	8×10^{-17}	3×10^{-18}	3×10^{-17}	9×10^{-19}

Table 9. Standard uncertainty in the radiance temperature of a blackbody due to the correction for reflected ambient radiation. It is assumed in all cases that the ambient temperature is T_a = 20 °C. Normal values are for a blackbody emissivity of ε_{bb} = 0.999 and $u(\varepsilon_{bb})$ = 0.0006, and best for ε_{bb} = 0.99997 and. $u(\varepsilon_{bb})$ = 0.0001.

Description	Quantity	Probability distribution	Value / mK for λ=10 μm									
			–40 °C		–20 °C		50 °C		150 °C		500 °C	
			normal	best	normal	best	normal	best	normal	best	normal	best
Reflected ambient radiation	$u_6(T_i)$	normal	80	13	60	9.9	29	4.5	17	2.9	9.5	1.6

Description	Quantity	Probability distribution	Value / mK for λ=3.9 μm									
			20 °C		100 °C		200 °C		600 °C		960 °C	
			normal	best	normal	best	normal	best	normal	best	normal	best
Reflected ambient radiation	$u_6(T_i)$	normal	14	2.3	1.5	0.3	0.3	0.05	0.03	0.005	0.02	0.003

Description	Quantity	Probability distribution	Value / mK for λ=1.6 μm									
			150 °C		300 °C		500 °C		700 °C		960 °C	
			normal	best	normal	best	normal	best	normal	best	normal	best
Reflected ambient radiation	$u_6(T_i)$	normal	0.001	2×10^{-4}	7×10^{-6}	1×10^{-6}	2×10^{-7}	4×10^{-8}	3×10^{-8}	5×10^{-9}	7×10^{-9}	1×10^{-9}

Description	Quantity	Probability distribution	Value / mK for λ=0.9 μm									
			400 °C		600 °C		750 °C		960 °C		1085 °C	
			normal	best	normal	best	normal	best	normal	best	normal	best
Reflected ambient radiation	$u_6(T_i)$	normal	7×10^{-13}	1×10^{-13}	5×10^{-15}	9×10^{-14}	5×10^{-14}	8×10^{-17}	5×10^{-17}	8×10^{-18}	2×10^{-17}	3×10^{-18}

4.1.7 Heat Loss Effects

4.1.7.1 Radiant Heat Exchange

The loss of radiant energy through the aperture produces a temperature drop at the cavity bottom between the metal surface (FPBB scheme), or the contact sensor (VTBB scheme), and the inner cavity wall. Derived from [35, 36], an upper bound of the temperature drop caused by the radiant heat exchange and conductive heat flow can be calculated using the following formula:

$$\Delta T_b = \varepsilon_{tot}\ \sigma \left(T_i^4 - T_a^4\right) \frac{d}{\kappa} \left(\frac{r}{L}\right)^2 , \tag{25}$$

where ΔT_b is the temperature drop, ε_{tot} is the total emissivity of inner cavity wall, σ is the Stefan-Boltzmann constant, T_i is the blackbody temperature, T_a is the ambient temperature, d is the thickness of the cavity bottom, κ is the thermal conductivity of the cavity wall, possibly including a coating, r is the aperture radius, and L is the cavity length.

Table 10. Standard uncertainties of the blackbody temperature due to cavity bottom heat exchange.

Description	Quantity	Probability distribution	Value / mK					
			20 °C and below		500 °C		960 °C	
			normal	best	normal	best	normal	best
Cavity bottom heat exchange	$u_7(T_i)$	rectangular	0	0	15	5	105	35

The largest contribution to the uncertainty in this correction stems from the assumed value for the thermal conductivity and, partially, from the uncertainty in the thickness of the cavity bottom. Since the thermal conductivity of a cavity wall material sample (*inter alia*, graphite) depends on many physical and chemical factors, it is very difficult to compare values from different studies, or to predict what the value for a particular specimen is likely to be. The problem is made worse by much of the literature giving very little additional information about the samples; in particular, thermal conductivity values are often given without specifying the temperature at which they were measured. Manufacturers' data are not always reliable since a 'typical' value is usually quoted. Actual values can vary between samples of the same batch, as well as between specimens from one sample.

If an accurate value for the thermal conductivity of a sample is required, it is best to have it measured directly. It should be measured along the direction of interest to prevent errors due to anisotropy, as well as at the temperature(s) required. However, for this application, it is probably sufficient to estimate the value from the literature, or from the manufacturer's specifications. Providing the resulting uncertainty can be tolerated, values can also be extrapolated to different temperatures using a typical thermal conductivity temperature dependence. Details can be found in [37].

The contribution to the uncertainty budget is given in Table 10 for a cavity with diameter-to-length ratio of 1 to 10, a bottom wall thickness of 5 mm and an effective thermal conductivity of 15 W m^{-1} K^{-1}.

4.1.7.2 Convection Heat Loss

The uncertainty in the cavity temperature due to convection applies generally to the VTBB scheme. For blackbody cavities with large apertures ventilated to ambient air, convection in the cavity can lead to a deviation between the radiance temperature of the cavity and the temperature sensed by the reference thermometer, which is near the bottom of the cavity and in good thermal contact with the heat-transfer agent. Furthermore, at sub-ambient temperatures the formation of dew and ice on the cavity surface will increase the temperature gradient in the cavity wall and change the wall emissivity, further increasing this temperature deviation as a consequence. For fixed-point blackbodies the influence of convection on the uncertainty budget is negligible in most cases, due to the large length-to-aperture ratio of their cavities and the housing of the cavity with good thermal insulators.

The problem of convection has been studied in detail within the TRIRAT project [26]. In [38] two model fluid-bath blackbodies, which could be purged with dry nitrogen regulated to the bath temperature by carrying the gas through the liquid, were investigated in the temperature range from –20 °C to 200 °C. The change in radiance temperature, while changing the nitrogen flow rate from zero to the maximum value of 5 *l*/min, was measured for different temperatures. Similar investigations are reported in [39] on two fluid-bath blackbodies. Additionally, in [39] the heat-exchange effect was studied by initially covering the cavity opening with a lid of synthetic rubber and subsequently removing the lid to allow air convection to occur while measuring the radiance temperature as convection progressed. In [38] and [39] blackbodies of comparable cavity length, but with different aperture diameters (60 mm diameter in [38] and 20 mm diameter in [39]), were measured. The influence of convection found in [38] was, therefore, larger than in [39], but the results in both investigations were of the same order of magnitude and their development with the cavity temperature was identical. In [38] the investigations on convection were extended to ammonia and water heat-pipe blackbodies, both equipped with a nitrogen purging system. The temperature of the nitrogen was equalised to the cavity temperature by conducting the gas flow through the heat pipe before it entered the cavity through a ring of small holes in the cavity wall near the aperture of the heat pipe. Additionally, for a caesium and a sodium heat pipe, the influence of convection on the temperature uniformity of the cavity bottom was investigated for different apertures.

In summary, conclusions from these measurements are:

- For large-aperture blackbodies without temperature-controlled gas purging systems (normal accuracy), convection may lead to a significant deviation of the radiance temperature from the reading on the reference thermometer sensing the temperature of the heat-transfer agent. The magnitude of the temperature difference depends on the cavity temperature, the cavity geometry, and the thermal resistance between the heat-transfer agent and the inner

surface of the cavity bottom. The temperature deviation is more pronounced for operation below ambient temperature than for operation above ambient temperature.

- For large-aperture blackbodies with purging systems (best accuracy), the influence of convection can be sufficiently suppressed with a gas flow rate typically >3 *l*/min. Most efficient is the purging of gas through an inlet close to the opening of the cavity. To prevent the build up of ice at sub-zero temperatures, a gas flow rate of typically >5 *l*/min is necessary. If no purging system is applied, the influence of convection is diminished by moving the position of the aperture further back into the furnace and applying an additional protection tube in front of the furnace opening.
- At temperatures above 270 °C, purging systems are not applied with large-aperture blackbodies. For the caesium and sodium heat-pipe blackbodies, experiments have shown that the use of apertures of 30 mm diameter or smaller with a cavity length of 370 mm and the insertion of the cavity opening into the furnace by 90 mm sufficiently diminishes convection heat losses [38].

The uncertainties are summarised in Table 11.

Table 11. Standard uncertainties estimated for on-axis observations of a heat-pipe blackbody with an aperture of 60 mm diameter and a cavity length of 525 mm (normal: without purging; best: with purging). Above 270 °C, for best uncertainty, a 30 mm aperture, a cavity length of 370 mm, and no purging is assumed. Also, the cavity opening is moved 90 mm into the furnace.

Description	**Quantity**	**Probability distribution**	**Value / mK**					
			–30 °C		**–10 °C**		**0 °C**	
			normal	**best**	**normal**	**best**	**normal**	**best**
Convection	$u_8(T_i)$	rectangular	230	6	29	2	17	1

Description	**Quantity**	**Probability distribution**	**Value / mK**					
			23 °C		**23 °C to 50 °C**		**>50 °C to 150 °C**	
			normal	**best**	**normal**	**best**	**normal**	**best**
Convection	$u_8(T_i)$	rectangular	0	0	6	1	29	2

Description	**Quantity**	**Probability distribution**	**Value / mK**					
			>150 °C to 270 °C		**>270 °C to 500 °C 30 mm aperture**		**>500 °C to 960 °C 30 mm aperture**	
			normal	**best**	**normal**	**best**	**normal**	**best**
Convection	$u_8(T_i)$	rectangular	58	12	29	6	58	12

4.1.8 Cavity Bottom Uniformity

This component applies only to the VTBB scheme in practice. The uniformity of temperature along the bottom of radiators mainly depends on design features of the blackbody cavity including the heater/cooler element, and homogeneity of the material coating the bottom. The uniformity of a cavity bottom heated by electric sheath heaters tends to be much worse than by fluid baths or heat-pipes. Temperature non-uniformities can also be caused by conductive and convective heat flows and radiation loss through the aperture of the cavity, as discussed above. Non-uniformities directly affect the precision of calibrations even if comparisons of similar types of radiation thermometer are carried out.

A technique using a scanning laser probe beam to measure the emissivity of cavities [40] can be used as an indirect method to determine the cavity bottom uniformity. In this method an image of the effective reflectance and hence of emissivity (and hence of the radiance temperature) of the bottom of the blackbody cavity can be obtained, allowing the diagnosis of problems with cavity construction.

Table 12. Standard uncertainties of the blackbody temperature due to cavity bottom non-uniformity.

Description	Quantity	Probability distribution	Value / mK							
			–30 °C		20 °C		500 °C		960 °C	
			normal	best	normal	best	normal	best	normal	best
Cavity bottom uniformity	$u_9(T_i)$	normal	50	15	30	10	50	15	100	30

A direct method of measuring the cavity bottom uniformity is to translate a radiation thermometer with a small target area across the aperture. The distribution of readings across a central area of the bottom (40% to 60% of the area) can be used to calculate the standard uncertainty in the temperature uniformity [38] (see Table 12).

4.1.9 Ambient Conditions

The influence of ambient conditions on the uncertainty budget of a blackbody is identified with the noise of the radiance temperature of the blackbody. For fixed-point blackbodies this uncertainty is part of the uncertainty involved with the plateau identification, so this component only applies to the VTBB scheme. For large-aperture bath- and heat-pipe blackbodies this noise can be measured with a standard platinum resistance thermometer positioned close to the bottom of the cavity and in good thermal contact with the heat-transfer agent. For best accuracy, typical values of the standard deviation of the SPRT measurements of heat-pipe blackbodies with control loops of high temperature resolution (10 mK) are given in Table 13. For normal accuracy a control loop with a typical temperature resolution of 100 mK for compensation of the ambient conditions is assumed.

Table 13. Standard uncertainties in the radiance temperature of large-aperture blackbodies due to ambient conditions.

Description	Quantity	Probability distribution	Value / mK					
			–30 °C		–10 °C		0 °C	
			normal	best	normal	best	normal	best
Blackbody ambient conditions	$u_{10}(T_i)$	normal	58	10	58	9	58	9

Description	Quantity	Probability distribution	Value / mK					
			23 °C		23 °C to 50 °C		>50 °C to 150 °C	
			normal	best	normal	best	normal	best
Blackbody ambient conditions	$u_{10}(T_i)$	normal	58	8	58	7	58	3

Description	Quantity	Probability distribution	Value / mK					
			>150 °C to 270 °C		>270 °C to 500 °C		>500 °C to 960 °C	
			normal	best	normal	best	normal	best
Blackbody ambient conditions	$u_{10}(T_i)$	normal	58	7	58	5	58	12

4.2 Uncertainties Associated with the Radiation Thermometer

4.2.1 Size-of-Source Effect

At low temperatures, the size-of-source effect (SSE) is critically dependent on the operating wavelength of the radiation thermometer since the background radiation from the environment can be the dominant portion of the total radiation incident on the detector. This discussion of the SSE is thus divided into radiation thermometers in the near-infrared (NIR) at 0.9 μm and 1.6 μm, mid-infrared (MIR) at 3.9 μm, and the thermal-infrared (TIR) at 10 μm.

4.2.1.1 Near Infrared

Radiation thermometers in the NIR typically utilise silicon or indium gallium arsenide (InGaAs) detectors often with thermoelectric cooling for temperature stabilisation. Since the background radiation at this wavelength is negligible, the SSE characterisation/correction is similar to shorter wavelength radiation thermometers utilising silicon diodes in the visible [1].

The SSE function can be measured using either the "direct" method, in which the radiation thermometer under test views a uniform circular source of varying diameter, or the "indirect" method, in which it views the same source but with a central obscuration slightly larger than the target size [41]. The two methods have been found to be comparable [42]. The SSE function can be defined as

$$\sigma(D, D_0) = \frac{S(L, D) - S(L, D_0)}{S(L)}, \tag{26}$$

where D is the diameter of a uniform radiance source, D_0 is an arbitrary reference diameter, and L is the radiance of the source. For the indirect method D_0 can be the diameter of the central obscuration. In this case, the signal measured while viewing the unobstructed radiance source is $S(L)$, and the signal measured while viewing the central obscuration with the diameter of the radiance source, D, is $S(L, D)$. The signal measured with the diameter of the variable aperture at the diameter of the central obscuration, D_0, is $S(L, D_0)$. The SSE correction is found from the product of the differential increase in the SSE and the measured relative spatial distribution of the radiance, $L(D)/L_0$, of the source under measurement [43]:

$$\sigma_{\text{corr}}(D_0) = \int \frac{L(D)}{L_0}\left[\frac{d\sigma(D, D_0)}{dD}\right] dD\,. \tag{27}$$

Since regular lenses transmit in this wavelength region, the design of radiation thermometers can be made the same as for radiation thermometers utilising Si diodes in the visible [1]. The SSE is found to be dependent on the design of the radiation thermometer [44], and whether a Lyot stop is present [45] or a simple single lens configuration is used [6]. The SSE comparisons in Table 14 are from the TRIRAT document [26].

4.2.1.2 Mid-Infrared and Thermal Infrared

For mid- and thermal infrared thermometers, the SSE can have a large contribution to the signal because the relative radiance of the source outside the nominal source diameter is large. The signal of a source of diameter D with radiance L and background radiance L_{back} can be described by a function $S(L, L_{\text{back}}, D)$. Since the SSE function can be measured only up to a finite diameter, D_{max}, of the measurement device, the reduced (or truncated) SSE function, σ', is given by

$$\sigma'(D, D_{\text{max}}) = \frac{S\left(L, 0, D\right)}{S\left(L, 0, D_{\text{max}}\right)} \tag{28}$$

using the direct method. A generalized description of the SSE corrections can be stated for a source of radiance L and diameter D_{actual}, measured under background radiance $L_{\text{back,actual}}$, corrected towards a source of the same radiance but with diameter D_0 and background radiation $L_{\text{back,0}}$:

$$\begin{aligned} S(L, L_{\text{back, 0}}, D_0) = {} & S(L, L_{\text{back, actual}}, D_{\text{actual}}) \\ & - \left[1 - \frac{\sigma'(D_0, D_{\text{max}})}{\sigma'(D_{\text{actual}}, D_{\text{max}})}\right]\left[S(L, L_{\text{back, actual}}, D_{\text{actual}}) - S(L_{\text{back, actual}}, \infty)\right] \\ & + \left[1 - \sigma'(D_0, D_{\text{max}})\right]\left[S(L_{\text{back, 0}}, \infty) - S(L_{\text{back, actual}}, \infty)\right]. \end{aligned} \tag{29}$$

Table 14. Standard uncertainties due to the correction for SSE.

Description	Quantity	Prob. dist.	Value		Equivalent temperature uncertainty / mK							
			normal	best	20 °C, λ=10 µm		500 °C, λ=3.9 µm		500 °C, λ=1.6 µm		750 °C, λ=0.9 µm	
					normal	best	normal	best	normal	best	normal	best
SSE	$\sigma(\rho, r_0)$		0.015 (TIR) 0.015 (MIR) 0.003 (NIR)	0.006 (TIR) 0.004 (MIR) 0.0005 (NIR)								
SSE measurement	$\frac{u(\sigma)}{\sigma}$	rect.	0.0005	0.00001	32	0.6	80	1.6	33	0.7	33	0.7
Radiance distribution	$\frac{u(L)}{L_0}$	rect.	0.0005	0.00001	32	0.6	80	1.6	33	0.7	33	0.7
SSE correction	$\frac{u_{11}(S_i)}{S_i}$	**rect.**	**0.0007**	**0.000014**	**44**	**0.9**	**113**	**2.3**	**46**	**0.9**	**46**	**0.9**

In equation (29), (for infinitely large source diameter) L_{back} is irrelevant to $S(L, L_{\text{back}}, \infty)$ and the second parameter has been left out. Equation (29) is an approximation that holds if $L_{\text{back, actual}}$ is close enough to $L_{\text{back, 0}}$ or if $\sigma'(D_{\max}, \infty)$ is close enough to unity [46].

4.2.2 Non-linearity

Non-linearity (NL) can arise from the intrinsic property of the detector or from the system characteristics of the electronic circuit used to measure the radiation. Thus, if possible, measurements of non-linearity should be performed with the detector integrated into a system and not characterised separately.

Non-linearity can be measured using a variety of methods, often described as either "dual aperture" or "superposition" methods. The non-linearity data can be analysed either cumulatively or combinatorially depending on the method used [47]. The most common measurement technique builds up the non-linearity cumulatively [48]:

$$\mathrm{NL}(S_{A+B}) = \frac{S_A + S_B}{S_{A+B}}, \tag{30}$$

where the signals from the individual paths are S_A and S_B, and the combined-path signal is S_{A+B}. When $S_A = S_B$, this is known as the flux doubling technique. The non-linearity is cumulative since the signals S_A and S_B may themselves be non-linear.

Combinatorial techniques determine a direct relationship between flux and measured signal by combining fixed fluxes from at least two paths in a variety of different combinations. This relationship can be modelled, for example, by [49]

$$\phi(i,j,k) = \phi(i,j) + \phi(j,k) = r_0 + S(i,j,k) + r_2 S^2(i,j,k) + \ldots + r_n S^n(i,j,k), \tag{31}$$

where $\phi(i,j,k)$ denotes the total flux, $S(i,j,k)$ the measured signal at the detector, and r_0, r_2, …, r_n are coefficients that relate the signal to the flux. The i, j, and k indices label the different flux combinations, and refer, for example, to settings on different filter wheels in the flux paths. The total flux at the detector is the sum of the individual fluxes, $\phi(i,j)$ and $\phi(j,k)$, where flux addition is inherently linear. Redundancy in the number of measurements allows the r coefficients to be determined. The non-linearity is obtained from the total flux and the signal:

$$\mathrm{NL}(S) = \frac{\phi(i,j,k)}{S(i,j,k)}. \tag{32}$$

In both methods, the signals are corrected by using

$$S_{\text{corrected}} = \mathrm{NL} \times S_{\text{uncorrected}}. \tag{33}$$

In the near-infrared wavelength region at 1.6 μm, the detector material with the highest shunt resistance is InGaAs, and is the preferred detector in radiation thermometers operating at this wavelength. InGaAs has been found to be non-linear with overfilling of the diode with radiation [50, 51] and is found to be linear with underfilling of the diode [52, 53].

For MIR radiation thermometers centred on 3.9 μm with a delta function spectral width, the ratio of Planck radiances can range from modest values like L(800 °C) / L(157 °C) = 176, to demanding ratios like L(960 °C) / L(20 °C) = 15500, which is outside the range of linear behaviour for radiation thermometers utilising indium antimonide (InSb) detectors [54]. For the 8 μm to 14 μm TIR radiation thermometer, the ratio of expected signals, S(300 °C) / S(–40 °C) = 35, is within the range of linear behaviour for radiation thermometers utilising mercury cadmium telluride (HgCdTe or MCT) detectors in photovoltaic mode [55]. In contrast, a ratio S(500 °C) / S(–40 °C) = 72 is again outside the linear operation range. Table 15 summarises a generalised estimation of the resulting uncertainties in the four wavelength ranges after correcting for non-linearity.

For mid- and thermal infrared radiation thermometers, the measurements referred to above are all detector based. Measurement as an integrated instrument has not yet been conducted, due to difficulty in measurements where all optical components such as beam splitters or shutters become radiators. Also the difficulty in determining the zero signal level in the presence of heavy background radiation must be given due thought.

Table 15. Standard uncertainties due to the measurement and correction of the non-linearity.

Description	Quantity	Prob. dist.	normal	best	Equivalent temperature uncertainty/ mK	
					normal	best
Non-linearity	$\frac{u_{12}(S_i)}{S_i}$	normal	**Value for λ=10 μm**		**20 °C**	
			2×10^{-3}	2×10^{-4}	130	13
Non-linearity	$\frac{u_{12}(S_i)}{S_i}$	normal	**Value for λ=3.9 μm**		**150 °C**	
			1×10^{-3}	1×10^{-4}	50	4.9
Non-linearity	$\frac{u_{12}(S_i)}{S_i}$	normal	**Value for λ=1.6 μm**		**500 °C**	
			6×10^{-4}	0	40	0
Non-linearity	$\frac{u_{12}(S_i)}{S_i}$	normal	**Value for λ=0.9 μm**		**750 °C**	
			5×10^{-4}	0	33	0

4.2.3 Effect of Instrument Temperature

At low temperatures, the uncertainties associated with the radiation thermometer are complicated by the fact that the temperature of the instrument is close to or even higher than the temperature of the measurement object. For thermal detectors the net signal detected by the thermometer is equal to the difference between the signal at the source radiance temperature, T, and the signal at some reference temperature, T_{ref} [56]:

$$S_{\mathrm{net}} = S(T) - S(T_{\mathrm{ref}}) \,. \tag{34}$$

The reference temperature is either the temperature of the detector, which may be ambient temperature for the less expensive thermometers, or the temperature of a reference surface for chopped systems. It is important to note that no signal is generated when the reference and source temperatures are the same. Well above the reference temperature, only radiation from the source is important, but below about 200 °C the contribution at the reference temperature is important. The thermometer and its electronics calculate the signal at the source temperature, $S(T)$, by adding to the net detected signal a correction equal to the signal at reference temperature. This requires the reference temperature to be measured.

Quantum detectors for mid- or thermal infrared detection are usually cooled. Even for such instruments, the detector radiation is reflected back internally to the detector contributing to the signal, and the temperature fluctuation of the detector contributes to the uncertainty. The optics, such as lenses, mirrors or baffles, are radiating sources. Instruments are usually operated in AC mode to eliminate these effects, but what is placed in between the chopper and the measurement object still contributes to the signal.

The detected signal, S_{det}, for quantum or thermal detectors in AC mode is described by

$$S_{\text{det}} = \left[S(L) + S_1' + S''\right] - \left[S_1' + S_2'\right], \tag{35}$$

where $S(L)$ is the signal from the measurement object that we want to detect, S_1' accounts for the signal eliminated by the chopping, such as self-radiation of the detector or internal radiation of the housing inside the chopping system. S'' accounts for the radiation originating from outside the chopping system, which is, therefore, chopped and cannot be eliminated. Radiation from the lens or mirror optics is such a source. S_2' is the signal that is subtracted in excess, such as the chopper wheel's apparent radiance contribution, including the chopper wheel radiation and the reference cavity radiation (at T_{ref}) reflected off the chopper wheel. The first group on the right hand side of this equation describes the signal when the chopper wheel does not obstruct the viewing of the object. The second group is the signal when it does. For DC operated systems, the second group on the right hand side is absent. For thermal detectors in DC mode, the detector temperature T_{ref} is the most critical. For the quantum or thermal detectors in AC mode, S_2' is the most critical.

4.2.3.1 Reference Temperature

For thermal detectors, or quantum detectors in AC mode, the reference temperature must be internally measured in order to correct for $S(T_{\text{ref}})$ in equation (34) or S_2' in equation (35). An error, ΔT_{ref}, in the measurement of the reference temperature leads to a relative signal error of

$$\frac{\Delta S(T_i)}{S(T_i)} = \frac{S(T_{\text{ref}})}{S(T_i)} \frac{c_2 \Delta T_{\text{ref}}}{T_{\text{ref}}^2 \lambda_{T_{\text{ref}}} \left[1 - \exp\left(-c_2 / \lambda_{T_{\text{ref}}} T_{\text{ref}}\right)\right]} \approx 0 \text{ when } T_{\text{ref}} \ll T_i \,. \tag{36}$$

This can be substituted into equation (7) to convert it into a temperature error. Table 16 illustrates standard uncertainty values for a reference temperature of 20 °C, where the normal values are for an uncertainty of 0.1 °C in the measurement of T_{ref}, and best are for an uncertainty of 0.01 °C.

Table 16. Standard uncertainties due to the measurement of T_{ref}.

Description	**Quantity**	**Probability distribution**	**Value / mK**							
			20 °C, λ=10 μm		**150 °C, λ=3.9 μm**		**λ=1.6 μm**		**λ=0.9 μm**	
			normal	**best**	**normal**	**best**	**normal**	**best**	**normal**	**best**
Reference temperature	$u_{13}(T_i)$	normal	100	10	4.4	0.44	0	0	0	0

4.2.3.2 Ambient Temperature

In order to make corrections, the drift in internal temperature of the instrument needs to be monitored and a predetermined correction factor applied. It is usually not possible to independently characterise the correction factors for various sources of background radiation, so they are all treated as a net effect.

This net effect, characterised by changing the ambient temperature, will be comprised of the following:

- Change in background radiation;
- Change in detector responsivity due to change in detector temperature;
- Temperature dependence of the amplifier;
- Temperature shift of the optical filter wavelength.

This corresponds to contributions from thermometer parts (detector, reference source, amplifier, optics, etc.) due to change in ambient temperature. For temperature controlled parts, this is through temperature fluctuations from the controller set temperature. For parts that are not controlled but are temperature monitored for correction, this accounts for the correction error. For uncontrolled and uncorrected parts, this is simply the thermal drift. The net effect for these is treated here.

The dependence of a 1.6 μm radiation thermometer's signal, S, to ambient temperature, T_a, has been characterised inside a walk-in temperature chamber at the zinc freezing point temperature. The ambient temperature was changed from

20 °C to 27 °C for this characterisation. In addition, the ambient temperature dependence was assessed as a function of radiance temperature measured at the Zn and Al points. The value of $(\Delta S/S)/\Delta T_a$ was found to be independent of radiance temperature and corresponded to $(\Delta S/S)/\Delta T = 1.5\times10^{-4}$ °C^{-1} at the Zn point.

Literature has shown that for thermometers at 3.9 µm, the ambient temperature dependence is about 8×10^{-5} °C^{-1} at 800 °C [57] (equivalent to 25 mK °C^{-1}). This is slightly more than at 1.6 µm, which corresponds to about 20 mK °C^{-1} at 800 °C.

For the 8 µm to 14 µm thermometer, a large dependence of the SSE on ambient temperature has been reported [46]. Assuming that the ambient temperature change affects the slope of the curve in Figure 3 of reference [46] and that the uncertainty in the thermometer signal corresponds to 5 % of the SSE correction, gives $(\Delta S/S)/\Delta T = 1\times10^{-3}$ °C^{-1}.

A change in the relative uncertainty in the detector sensitivity of $u(\Delta S/S)$ results in a relative signal error of

Table 17. Standard uncertainties due to variations in ambient temperature, assuming a reference temperature of 20 °C.

Description	**Quantity**	**Prob. dist.**	**normal**	**best**	**Equivalent temperature uncertainty/ mK for λ=10 µm at –20 °C**	
Detector sensitivity	$u\left(\frac{\Delta S}{S}\right)$	normal	**Value for λ=10 µm**			
			1×10^{-3}	1×10^{-4}		
Ambient temperature	$\frac{u_{14}(S_i)}{S_i}$	normal	**Value for λ=10 µm at –20 °C**		**normal**	**best**
			1.1×10^{-3}	1.1×10^{-4}	51	5

Description	**Quantity**	**Prob. dist.**	**normal**	**best**	**Equivalent temperature uncertainty/ mK for λ=3.9 µm at 500 °C**	
Detector sensitivity	$u\left(\frac{\Delta S}{S}\right)$	normal	**Value for λ=3.9 µm**			
			8×10^{-5}	8×10^{-6}		
Ambient temperature	$\frac{u_{14}(S_i)}{S_i}$	normal	**Value for λ=3.9 µm at 500 °C**		**normal**	**best**
			8×10^{-5}	8×10^{-6}	13	1.3

Description	**Quantity**	**Prob. dist.**	**normal**	**best**	**Equivalent temperature uncertainty/ mK for λ=1.6 µm at 500 °C**	
Detector sensitivity	$u\left(\frac{\Delta S}{S}\right)$	normal	**Value for λ=1.6 µm**			
			1.5×10^{-4}	1.5×10^{-5}		
Ambient temperature	$\frac{u_{14}(S_i)}{S_i}$	normal	**Value for λ=1.6 µm at 500 °C**		**normal**	**best**
			1.5×10^{-4}	1.5×10^{-5}	10	1.0

Description	**Quantity**	**Prob. dist.**	**normal**	**best**	**Equivalent temperature uncertainty/ mK for λ=0.9 µm at 750 °C**	
Detector sensitivity	$\frac{u(s)}{s}$	normal	**Value for λ=0.9 µm**			
			2×10^{-4}	1.5×10^{-5}		
Ambient temperature	$\frac{u_{14}(S_i)}{S_i}$	normal	**Value for λ=0.9 µm at 750 °C**		**normal**	**best**
			2×10^{-4}	2×10^{-5}	13	1.3

$$\frac{u(S_i)}{S_i} = u\left(\frac{\Delta S}{S}\right)\left[1 - \frac{S(T_{\text{ref}})}{S(T_i)}\right] \approx u\left(\frac{\Delta S}{S}\right) \text{ when } T_{\text{ref}} \ll T_i\,, \tag{37}$$

where T_{ref} is the temperature of the detector or of the reference cavity. This can be converted into a temperature uncertainty by substituting equation (37) into equation (7). Table 17 gives the uncertainties due to ambient temperature assuming there is no dependence of $(\Delta S/S)/dT$ on radiance temperature, and that $T_{\text{ref}} = 20$ °C. Normal values are for an ambient temperature stability of ±1 °C and best for a stability of ±0.1 °C.

4.2.4 Atmospheric Absorption

The effects of atmospheric absorption and emission are equivalent to a change in the net signal detected by the radiation thermometer. Atmospheric water vapour and carbon dioxide are the most commonly encountered gas species affecting absorption and emission in the infrared in most applications. Application of a computed correction for these absorption and emission effects is rarely practical. The best approach to deal with such problems is to use a non-absorbing spectral band (atmospheric window), which avoids both absorption of target radiation and emission from the atmosphere itself. This usually requires relatively narrow bandwidths. Working distance is another consideration as the absorption is proportional to the path length of the target radiation.

Standard radiation thermometers in low-temperature measurement, whether in NIR, MIR or TIR, always work in an atmospheric window with very narrow bandwidths in indoor laboratory conditions. The target distance is seldom longer than 1 m. In this case, the absorption and emission effects are negligible. It is hard to estimate the uncertainty on this as experimental data are seldom available. The only published experimental study found is an experiment using an IR camera [58]. The IR camera was tested for MIR (3 μm to 5 μm) and TIR (8 μm to 12 μm) at a blackbody temperature of about 90 °C and working distances from 0.5 m to 20 m. Assuming that there was no effect at 0.5 m target distance, the measurement results showed that the absorption effect was less than 0.1 % and 0.03 % at a target distance of 1 m for MIR and TIR, respectively. In principle, the effect on the IR camera used would be much larger than a standard radiation thermometer with narrow bandwidth, especially in the spectral range from 3 μm to 5 μm where there are absorption lines. For example, a standard radiation thermometer with narrow spectral band at 3.9 μm can avoid these absorption lines. As a conclusion, one can probably take 0.03 % as a very pessimistic estimation of uncertainty in the normal case (see Table 18).

Table 18. Standard uncertainties due to atmospheric absorption.

Description	**Quantity**	**Prob. dist.**	**Value**		**Equivalent temperature uncertainty / mK**							
					20 °C, λ=10 μm		**500 °C, λ=3.9 μm**		**500 °C, λ=1.6 μm**		**750 °C, λ=0.9 μm**	
			normal	**best**	**normal**	**best**	**normal**	**best**	**normal**	**best**	**normal**	**best**
Atmospheric absorption	$\frac{u_{15}(S_i)}{S_i}$	normal	0.0003	0.0001	19	6.3	48	16	20	6.6	20	6.6

4.2.5 Gain Ratios

The uncertainty in gain ratios for a 1.6 μm thermometer has been assessed. There are three parameters considered in the determination of the uncertainty due to gain ratios:

- Short-term stability of the single gain at the specific output.
- Stability of the single gain, regardless of the output voltage range.
- Determination of the each gain ratio in the full operating range.

The thermometer signal changes by 6 orders of magnitude for a 1.6 μm thermometer within the range 150 °C to 960 °C. For a 3.9 μm thermometer the signal changes by 4 orders of magnitude between 20 °C and 960 °C. For an 8 μm to 14 μm thermometer the signal changes by less than 2 orders of magnitude from –40 °C to 500 °C. Therefore, different gains are not required for the 8 μm to 14 μm thermometer, and it is only the short-term stability of the gain that leads to uncertainty in this case.

Table 19. Standard uncertainties due to uncertainties in gain ratios and short-term variations in gain.

Description	Quantity	Probability distribution	Value for λ=10 μm		Equivalent temperature uncertainty / mK at 20 °C	
			normal	best	normal	best
Gain ratios	$\frac{u_{16}(S_i)}{S_i}$	normal	1×10^{-4}	1×10^{-5}	6	0.6

Description	Quantity	Probability distribution	Value for λ=3.9 μm		Equivalent temperature uncertainty / mK at 500 °C	
			normal	best	normal	best
Gain ratios	$\frac{u_{16}(S_i)}{S_i}$	normal	1×10^{-4}	1×10^{-5}	16	1.6

Description	Quantity	Probability distribution	Value for λ=1.6 μm		Equivalent temperature uncertainty / mK at 500 °C	
			normal	best	normal	best
Gain ratios	$\frac{u_{16}(S_i)}{S_i}$	normal	6×10^{-5}	6×10^{-6}	4	0.4

Description	Quantity	Probability distribution	Value for λ=0.9 μm		Equivalent temperature uncertainty / mK at 750 °C	
			normal	best	normal	best
Gain ratios	$\frac{u_{16}(S_i)}{S_i}$	normal	1×10^{-5}	2×10^{-6}	0.6	0.1

4.2.6 Noise

The noise of the signal is evaluated as a type A uncertainty. The contribution of this source of uncertainty can become considerably large when measuring close to the lower limit of the instrument measurement temperature range. Also the signal can become noisy due to quantisation error of the signal. It is important when sampling the noise contribution to ensure than none of the effects discussed above are included, otherwise "double-counting" will occur. Sources of noise in detectors are discussed in [59]. Table 20 gives uncertainty values at specific temperatures. At lower temperatures, this increase in noise is usually compensated somewhat by a decrease in electrical bandwidth.

Table 20. Standard uncertainties due to noise equivalent temperature differences measured within one second.

Description	Quantity	Probability distribution	Value / mK							
			20 °C, λ=10 μm		500 °C, λ=3.9 μm		500 °C, λ=1.6 μm		750 °C, λ=0.9 μm	
			normal	best	normal	best	normal	best	normal	best
Noise	$u_{17}(T_i)$	normal	75	25	50	10	10	2	10	2

4.3 Interpolation Error

Interpolation error describes the difference between the temperature determined using an interpolation equation (e.g. equation (4)) and the temperature that would be calculated by integrating Planck's law over the spectral responsivity of the thermometer (equation (1)). In [60] it is shown that the interpolation error for radiation thermometers has the form of an *N*th-order polynomial, where there are *N* adjustable parameters in the interpolation equation:

$$\Delta T_{\text{int}} = E(x; r, B_1, B_2, \ldots)\lambda_0^{N-1}(T - T_1)(T - T_2)\ldots(T - T_N)\,. \tag{38}$$

The quantities λ_0, r, B_1, B_2, … are statistical properties of the thermometer's spectral responsivity, and $x = \lambda_0 T_{\text{m}}$, where T_{m} is the mean of the temperatures used to determine the parameters of the interpolation equation. λ_0 is the mean wavelength, $r = \sigma/\lambda_0$ is the relative bandwidth, $B_1 = \mu_3/\sigma^3$ is the skewness, $B_2 = \mu_4/\sigma^4$ is the kurtosis, and so on. σ is the standard deviation of the spectral responsivity, μ_3 and μ_4 are the third and fourth central moments, etc. The quantities B_1, B_2, … depend only on shape: for a rectangular spectral responsivity $B_1 = 0$ and $B_2 = 1.8$; for a Gaussian-shaped spectral responsivity $B_1 = 0$ and $B_2 = 3$. The coefficient E is, therefore, a constant for a given thermometer and set of calibration points. Equation (38) applies equally well to both interpolation (N equal to the number calibration points) and least-squares fitting (N less than the number of calibration points). The only difference between the two cases is the meaning of the temperatures T_1, T_2, …, T_N. For interpolation, these are equal to the calibration temperatures themselves. For least-squares fitting, they are N unspecified temperatures within the calibration range.

For the Sakuma–Hattori equation (4) (either the Wien or the Planck version), there are $N = 3$ parameters, so equation (38) becomes

$$\Delta T_{\text{int}} = E(x; r, B_1, B_2, \ldots)\lambda_0^2(T - T_1)(T - T_2)(T - T_3)\,. \tag{39}$$

As long as we restrict ourselves to the interpolation region (or a bit beyond), the maximum value of equation (39) is

$$\left|\Delta T_{\text{int}}\right|_{\text{max}} = \frac{|E|\lambda_0^2(T_3 - T_1)^3}{12\sqrt{3}}\,, \tag{40}$$

where $T_1 < T_2 < T_3$. We can assume conservatively that T_1 is the minimum calibration temperature and T_3 the maximum calibration temperature, so that equation (40) is proportional to the cube of the calibration range. Also, assuming $|\Delta T_{\text{int}}|_{\text{max}}$ represents the half range of a rectangular distribution gives a standard uncertainty due to interpolation for the entire calibration range of

$$u_{18} = \frac{|E|\lambda_0^2 T_{\text{range}}^3}{36}\,. \tag{41}$$

Values of $|E|$ for rectangular and Gaussian spectral responsivities are plotted in [60] for both Planck and Wien versions of the Sakuma–Hattori equation. The minimum value of $|E|$ for the Wien version of the Sakuma–Hattori equation is given by

$$|E|_{\text{min,Wien}} = \frac{c_2^2}{12x^4}\left[1 - \frac{1}{\left[1 - \exp(-c_2/x)\right]^2}\right], \tag{42}$$

where $x = \lambda_0 T_{\text{m}}$. The actual value of $|E|$ may be greater than this, but it is not possible to obtain a lower interpolation error without using the Planck version of the Sakuma–Hattori equation.

Table 21 shows the uncertainty due to interpolation error for both the Planck and Wien versions of the Sakuma–Hattori equation. For the 10 μm and 3.9 μm thermometers, there is a clear advantage in using the Planck version of the equation.

Table 21. Standard uncertainties due to interpolation error.

Description	**Quantity**	**Prob. dist.**	**Uncertainty contribution / mK**							
			λ=10 μm, –40 °C to 500 °C		**λ=3.9 μm, 20 °C to 960 °C**		**λ=1.6 μm, 150 °C to 960 °C**		**λ=0.9 μm, 400 °C to 1085 °C**	
			Wien	**Planck**	**Wien**	**Planck**	**Wien**	**Planck**	**Wien**	**Planck**
Interpolation error	u_{18}	Rect.	870	15	740	1.0	4.9	3.6	1.6	1.5

4.4 Drift

Drift in a calibrated radiation thermometer will produce an error in the temperature determined using the Sakuma–Hattori equation (4), since in effect the drift changes the values of the A, B, and C parameters. Most radiation thermometers are basically just filter radiometers, and their drift arises from: (i) the optical components, such as the lenses, mirrors, and windows; (ii) the radiation detector; and (iii) the electronics measuring the detector signal.

In general, most users determine the stability of their radiation thermometer by examining the drift between subsequent calibrations, and will use these experimentally determined values of drift. If the drift is large then it can be eliminated by re-determining the A, B, and C parameters using new calibration data. This section attempts to systematically examine the sources of drift in low-temperature radiation thermometers.

Detectors used for low-temperature radiation thermometers are limited by the available blackbody spectrum energy: Si detectors, with a band edge of 1100 nm are limited to 400 °C; uncooled InGaAs, with a band edge of 1600 nm are limited to about 150 °C; pyroelectrics, with broad-band response are usable down to –50 °C. Away from their band edge, the semiconductor detectors are generally extremely stable, with drifts of typically 0.1 %/yr, and as low as 0.02 %/yr. Near to the band edge the response generally becomes both very temperature sensitive and much more unstable. Pyroelectric detectors are less stable than photodiodes, with typical stability of 0.2 %/yr [61].

Drifts due to the optical components can be divided into shifts in transmission in the bandpass of the radiation thermometer and shifts in the effective wavelength. With proper care, window and lens transmission can be stable to better than 0.05 %, though cleaning etc can change transmission by up to a few tenths of a percent. For 10 μm devices, mirror optics are generally used, which have poorer stability than refractive components, typically about 0.5 % over a year.

The multilayer interference filters generally used to specify the bandpass of radiation thermometers have much greater internal losses and are, accordingly, more unstable, typically decreasing the signal by about 0.2 %/yr. Interference filters also exhibit a type of secular drift arising from the internal stresses generated during deposition. Although some manufacturers pre-anneal their filters, the residual stresses slowly anneal, and the physical dimensions of the interference filter slowly change. For good filters a rate of about 0.02 %/year is typical. This causes a drift in the mean wavelength of the filter, proportional to the wavelength, e.g. 0.1 nm/yr at 650 nm, but 0.3 nm/yr at 1600 nm, etc.

A change in the optical transmission from τ to $\tau + \Delta\tau$ is equivalent to a change in the C parameter of the Sakuma–Hattori equation by a factor $\Delta\tau/\tau$, which in turn is equivalent to a relative signal error of

$$\frac{\Delta S(T)}{S(T)} = \frac{\Delta\tau}{\tau}\left[1 - \frac{S(T_{\mathrm{ref}})}{S(T)}\right] \approx \frac{\Delta\tau}{\tau} \text{ when } T_{\mathrm{ref}} \ll T\,, \tag{43}$$

where T_{ref} is the temperature of the detector or of the reference cavity. Similarly, a change in detector sensitivity from s to $s + \Delta s$, is equivalent to a relative signal error of

$$\frac{\Delta S(T)}{S(T)} = \frac{\Delta s}{s}\left[1 - \frac{S(T_{\mathrm{ref}})}{S(T)}\right] \approx \frac{\Delta s}{s} \text{ when } T_{\mathrm{ref}} \ll T\,. \tag{44}$$

When the detector is at ambient temperature and source is near to the ambient temperature, shifts in filter transmission have less effect upon the calculated temperature, because any decrease in transmission is partially compensated by an increase in emission or reflection of ambient radiation. If the source and ambient temperatures are the same, the signal is totally insensitive to any changes.

A shift in the mean wavelength of the spectral responsivity (centre wavelength if the spectral responsivity is symmetrical) from λ_0 to $\lambda_0 + \Delta\lambda_0$ causes a change in both the A and the C parameters of the Sakuma–Hattori equation. For mechanical annealing processes in interference filters, the bandwidth of the filter also increases proportionally to the drift in the filter wavelength. The B parameter remains unchanged, since it is proportional to the square of the relative bandwidth [62]. Therefore, a change in the mean wavelength is equivalent to a relative signal error of

$$\frac{\Delta S(T)}{S(T)} = \frac{\Delta\lambda_0}{\lambda_0}\left\{\frac{c_2}{T\lambda_T\left[1-\exp\left(-c_2/\lambda_T T\right)\right]} - \frac{S(T_{\text{ref}})}{S(T)}\frac{c_2}{T_{\text{ref}}\lambda_{T_{\text{ref}}}\left[1-\exp\left(-c_2/\lambda_{T_{\text{ref}}}T_{\text{ref}}\right)\right]} - 5\left[1-\frac{S(T_{\text{ref}})}{S(T)}\right]\right\}$$
$$\approx \frac{\Delta\lambda_0}{\lambda_0}\left\{\frac{c_2}{T\lambda_T\left[1-\exp\left(-c_2/\lambda_T T\right)\right]} - 5\right\} \text{ when } T_{\text{ref}} \ll T. \quad (45)$$

A summary of drift sources in is given in Table 22. The corresponding temperature uncertainty components, obtained by substituting each of equations (43) to (45) into an equation similar to equation (7), are given in Table 23 for a reference temperature of 20 °C.

Table 22. Standard uncertainties in radiation thermometer properties that lead to drift over a period of one year.

Description	**Quantity**	**Prob. Dist.**	**Value**							
			λ=10 µm		**λ=3.9 µm**		**λ=1.6 µm**		**λ=0.9 µm**	
			normal	**best**	**normal**	**best**	**normal**	**best**	**normal**	**best**
Window transmission/ mirror reflectance	$\frac{u(\tau)}{\tau}$	normal	0.005	0.002	0.001	0.0005	0.001	0.0005	0.001	0.0005
Filter transmission	$\frac{u(\tau)}{\tau}$	normal	0.002	0.001	0.002	0.001	0.002	0.001	0.002	0.001
Detector sensitivity	$\frac{u(s)}{s}$	normal	0.002	0.001	0.002	0.001	0.001	0.0002	0.001	0.0002
Mean wavelength	$\frac{u(\lambda_0)}{\lambda_0}$	normal	0.0003	0.0001	0.0003	0.0001	0.0003	0.0001	0.0003	0.0001

Table 23. Standard uncertainties in radiance temperature due to drift over a period of one year. The reference temperature is assumed to be ambient at 20 °C.

Description	**Quantity**	**Prob. Dist.**	**Value / mK**							
			–20 °C, λ=10 µm		**500 °C, λ=3.9 µm**		**500 °C, λ=1.6 µm**		**750 °C, λ=0.9 µm**	
			normal	**best**	**normal**	**best**	**normal**	**best**	**normal**	**best**
Window transmission/ mirror reflectance	$u_\tau(T)$	normal	256	102	161	80	66	33	66	33
Filter transmission	$u_\tau(T)$	normal	102	51	322	161	132	66	132	66
Detector sensitivity	$u_s(T)$	normal	102	51	322	161	66	13	66	13
Mean wavelength	$u_{\lambda_0}(T)$	normal	14	4.8	9.5	3.2	133	44	209	70
Drift	$\boldsymbol{u_{18}(T)}$	**normal**	**294**	**125**	**483**	**241**	**209**	**87**	**264**	**103**

5. Propagation of Uncertainty Calculations

5.1 Interpolation

For interpolation ($N = 3$), the sensitivity coefficients $\partial S(T)/\partial T_i$ and $\partial S(T)/\partial S_i$ in equation (5) are given by [7]

$$\frac{\partial S(T)}{\partial T_i} = -\frac{\partial S(T)}{\partial T}\bigg|_{T=T_i} \sum_{j=1}^{3} \mathbf{M}^{-1}_{i,j} \frac{\partial S(T)}{\partial a_j} \tag{46}$$

and

$$\frac{\partial S(T)}{\partial S_i} = \sum_{j=1}^{3} \mathbf{M}^{-1}_{i,j} \frac{\partial S(T)}{\partial a_j} \tag{47}$$

where $a_1 \equiv A$, $a_2 \equiv B$, $a_3 \equiv C$, and $\mathbf{M}^{-1}_{i,j}$ is the (i,j)th element of the inverse of the 3×3 matrix $\mathbf{M}$, whose elements are given by

$$\mathbf{M}_{i,j} = \frac{\partial S(T)}{\partial a_i}\bigg|_{T=T_j} . \tag{48}$$

The full analytic expressions for the sensitivity coefficients are somewhat unwieldy (see expression (51) below), although they can be calculated numerically easily enough. However, if we use the Wien approximation to equation (4) (i.e. neglect the –1) then the sensitivity coefficients have a very simple form and equation (5) simplifies to:

$$u_c^2(T) = \sum_{i=1}^{3} \Big[L_i(T) u(T_i) \Big]^2 + \sum_{i=1}^{3} \left[L_i(T) \frac{\lambda_{T_i} T_i^2}{c_2} \frac{u(S_i)}{S_i} \right]^2 , \tag{49}$$

where $L_i(T)$ are Lagrange polynomials in T of order 2:

$$L_i(T) = \frac{\prod_{j=1, j\neq i}^{3} (T - T_j)}{\prod_{j=1, j\neq i}^{3} (T_i - T_j)} , \text{ e.g. } L_1(T) = \frac{(T - T_2)(T - T_3)}{(T_1 - T_2)(T_1 - T_3)} , \tag{50}$$

and λ_{T_i} is the limiting effective wavelength, λ_T, evaluated at T_i. The Lagrange polynomials have a type of orthonormality property, namely $L_i(T_j) = 1$ when $j = i$ and $L_i(T_j) = 0$ when $j \neq i$. This leads to the validity of equation (8) at the calibration points.

Although the Planck version of equation (49) is rather more complicated, the orthonormality property still holds, leading to equation (7). For example, for the $i = 1$ terms of equation (49), in place of $L_1(T)$, the Planck version has

$$\frac{T^2(T_3 - T_2)\big[A^2 - \lambda_x^2(T)P(T)\big] + T_2^2(T - T_3)\big[A^2 - \lambda_x^2(T_2)P(T_2)\big] + T_3^2(T_2 - T)\big[A^2 - \lambda_x^2(T_3)P(T_3)\big]}{T_1^2(T_3 - T_2)\big[A^2 - \lambda_x^2(T_1)P(T_1)\big] + T_2^2(T_1 - T_3)\big[A^2 - \lambda_x^2(T_2)P(T_2)\big] + T_3^2(T_2 - T_1)\big[A^2 - \lambda_x^2(T_3)P(T_3)\big]} , \tag{51}$$

where $\lambda_x(T)$ is equation (3) evaluated at temperature T, and $P(T) = \exp\big[-c_2/\lambda_x(T)T\big]$. The ith term in the second summation of equation (49) also has the additional multiplying factor $\Big[1 - \exp\Big(-c_2/\lambda_{T_i} T_i\Big)\Big]$ in the Planck version. Under the usual conditions for which Wien's approximation to Planck's law is valid, the expression (51) collapses down to the Lagrange polynomial $L_1(T)$.

5.2 Least-Squares Fitting

When $N > 3$, that is when least-squares fitting is used to determine the A, B, and C parameters of equation (4), the sensitivity coefficients used in equation (5) are different. They are given by [7]

$$\frac{\partial S(T)}{\partial T_i} = \sum_{j=1}^{3} \left[\mathbf{B}\mathbf{H}^{-1} \right]_{i,j} \frac{\partial S(T)}{\partial a_j} \tag{52}$$

and

$$\frac{\partial S(T)}{\partial S_i} = \sum_{j=1}^{3} \left[\mathbf{C}\mathbf{H}^{-1} \right]_{i,j} \frac{\partial S(T)}{\partial a_j}, \tag{53}$$

where $[\mathbf{B}\mathbf{H}^{-1}]_{i,j}$ is the $(i,j)^{\text{th}}$ element of the product of the two matrices $\mathbf{B}$ and $\mathbf{H}^{-1}$, and $[\mathbf{C}\mathbf{H}^{-1}]_{i,j}$ is the $(i,j)^{\text{th}}$ element of the product of $\mathbf{C}$ and $\mathbf{H}^{-1}$. The matrix elements of the $N \times 3$ matrix $\mathbf{B}$ are

$$\mathbf{B}_{i,j} = -w_i \left(\frac{\partial S(T)}{\partial T} \frac{\partial S(T)}{\partial a_j} \right)\Bigg|_{T=T_i} + w_i \left[S_i - S(T_i) \right] \frac{\partial^2 S(T)}{\partial T \partial a_j}\Bigg|_{T=T_i} \quad (i = 1,2,...,N,\ j = 1,2,3)\ , \tag{54}$$

and those of the $N \times 3$ matrix $\mathbf{C}$ are

$$\mathbf{C}_{i,j} = w_i \frac{\partial S(T)}{\partial a_j}\Bigg|_{T=T_i} \quad (i = 1,2,...,N,\ j = 1,2,3)\ . \tag{55}$$

The matrix elements of the 3×3 matrix $\mathbf{H}$ are

$$\mathbf{H}_{i,j} = \sum_{k=1}^{N} w_k \left(\frac{\partial S(T)}{\partial a_i} \frac{\partial S(T)}{\partial a_j} \right)\Bigg|_{T=T_k} \quad (i = 1,2,3,\ j = 1,2,3)\ . \tag{56}$$

The w_i values are weights used for the least-squares fit, and are given by

$$w_i = \left[u^2(S_i) + \left(\frac{\partial S(T)}{\partial T}\Bigg|_{T=T_i} u(T_i) \right)^2 \right]^{-1}\ . \tag{57}$$

Note that because of the residual terms, $S_i - S(T_i)$, appearing in equation (54), the relationship between signal uncertainties and temperature uncertainties, given by equation (7) or (8), does not hold exactly at the calibration points.

Least-squares fitting provides a reduction in the combined uncertainty over interpolation by a factor of about $\sqrt{3/N}$.

5.3 Inclusion of In-Use Uncertainty Components

In equation (6) we included in the total uncertainty the term $u_{20}(T)$, which contains a multitude of components that occur when the radiation thermometer is used to measure an unknown temperature, T, subsequent to the calibration. In general, $u_{20}(T)$ will depend on the nature of the source and its surroundings, as well as properties of the thermometer already discussed in the above sections. In some cases $u_{20}(T)$ may dominate the total uncertainty. Most of the components of $u_{20}(T)$ will represent uncertainties in signal, which propagate according to

$$u(T) = \frac{\lambda_T T^2 \left[1 - \exp\left(-c_2 / \lambda_T T \right) \right]}{c_2} \frac{u(S)}{S}\ . \tag{58}$$

In the Wien approximation, this reduces to

$$u(T) = \frac{\lambda_T T^2}{c_2} \frac{u(S)}{S}\ . \tag{59}$$

5.3.1 Non-Linearity Components

The complication with equation (6) is that many of the uncertainty terms arising during calibration will be highly correlated with the corresponding components of $u_{20}(T)$ during use. An example is the uncertainty in the correction for non-linearity, which originates largely from the method used to measure non-linearity and becomes non-random when corrections are applied. That is, the uncertainties in the measurements made to determine non-linearity affect the thermometer signal during both calibration and use in the same way. In order to avoid dealing directly with correlations, the errors in the non-linearity measurements must be propagated through both the calibration equation and the measurement at the unknown temperature simultaneously, before deriving the sensitivity coefficients for the non-linearity uncertainty. This requires removing the non-linearity component $u_{12}(S_i)/S_i$ from the $u(S_i)/S_i$ sum at each calibration point, and the corresponding non-linearity component from the $u_{20}(T)$ term of equation (6), and combining these components separately. It also requires a form for the function describing the non-linearity of the thermometer. This procedure, following [47], is described in the Appendix.

5.3.2 Other Components

Other components of $u_{20}(T)$ that are highly correlated with any of the calibration uncertainties can be treated in the same way as non-linearity described above, beginning with an underlying model. However, in most cases the correlations are zero, either because the effects arise from purely random events, such as short-term fluctuations in gain ratios, or that the conditions outside the radiation thermometer are different during calibration and use (for example, the blackbody sources may be different). In these uncorrelated cases, the components of $u_{20}(T)$ simply add in quadrature with those components arising from the calibration.

5.4 Uncertainty Plots

The typical normal and best total propagated uncertainty in the calibration of a radiation thermometer can be calculated using equation (6) and the information provided in the above tables once the calibration points have been chosen. Since there exist many combinations of different calibration temperatures, different numbers of calibration points, and different measurement schemes for each point, we give here only a few representative examples. In these examples, we do not include any of the in-use components other than non-linearity as discussed in Section 5.3.1. Thus, the uncertainties plotted here correspond only to calibration uncertainties.

Table 24 lists the uncertainty components for best accuracy for the FPBB scheme for a 1.6 μm thermometer using the three fixed points indium, aluminium, and silver. The quadrature sums at the bottom of each column are the values used in equation (5) to calculate the combined uncertainty from the calibration points. To this an interpolation error uncertainty, u_{18}, of 3.6 mK must be added for this thermometer, as well as the non-linearity component of equation (A5) in the Appendix. Equation (6) is plotted in Figure 1, along with the corresponding curves for normal accuracy for the FPBB scheme, and both normal and best accuracy for the VTBB scheme for three calibration temperatures of 150 °C, 550 °C, and 960 °C. The drift component, $u_{19}(T)$, is not included in these curves, so they represent the uncertainty immediately after calibration. Figures 2, 3 and 4 plot similar curves for a 0.9 μm thermometer, a 3.9 μm thermometer and an 8 μm to 14 μm thermometer, respectively.

In Figure 5 a comparison of the FPBB scheme at best accuracy for the four different thermometers is given. Figure 6 compares the uncertainty for a 3-point calibration using interpolation with a 4-point and 5-point least-squares calibration using the equations in Section 5.2, again neglecting drift. The drift component over one year is plotted in Figure 7. Assuming that drift occurs at a constant rate, a fraction of this curve should be added in quadrature to the curves in Figures 1 to 4 to obtain the total uncertainty.

Table 24. Standard uncertainty components for a 1.6 µm thermometer using a three-point FPBB scheme at best accuracy. The shaded cells are not applicable to the FPBB scheme. The totals at the bottom of the table are the quadrature sums of the corresponding column entries. For the signal uncertainty columns, the equivalent total temperature uncertainty is also given.

1.6 µm FPBB Scheme		**T_1 = 156.5985 °C**		**T_2 = 660.323 °C**		**T_3 = 961.78 °C**	
Description	***x***	**$u_x(T_1)$ / mK**	**$\frac{u_x(S_1)}{S_1}$**	**$u_x(T_2)$ / mK**	**$\frac{u_x(S_1)}{S_1}$**	**$u_x(T_1)$ / mK**	**$\frac{u_x(S_1)}{S_1}$**
Calibration temperature	1						
Impurities	2	0.3		0.4		0.7	
Plateau identification	3	2		2		2	
Blackbody emissivity, isothermal	4		0.0001		0.0001		0.0001
Blackbody emissivity, non-isothermal	5						
Reflected ambient radiation	6	0.0		0.0		0..0	
Cavity bottom heat exchange	7	0.0		5		35	
Convection	8						
Cavity bottom uniformity	9						
Ambient conditions	10						
Size-of-source effect	11		1.4×10^{-5}		1.4×10^{-5}		1.4×10^{-5}
Non-linearity	12		0.0		0.0		0.0
Reference temperature	13	0.0		0.0		0.0	
Ambient temperature	14		1.5×10^{-5}		1.5×10^{-5}		1.5×10^{-5}
Atmospheric absorption	15		0.0001		0.0001		0.0001
Gain ratios	16		6×10^{-6}		6×10^{-6}		6×10^{-6}
Noise	17	2		2		2	
Totals		**$u(T_1)$=2.8 mK**	**$\frac{u(S_1)}{S_1}$ = 0.00014 (2.9 mK)**	**$u(T_2)$=5.8 mK**	**$\frac{u(S_2)}{S_2}$ = 0.00014 (13.5 mK)**	**$u(T_3)$=35.1 mK**	**$\frac{u(S_3)}{S_3}$ = 0.00014 (23.6 mK)**

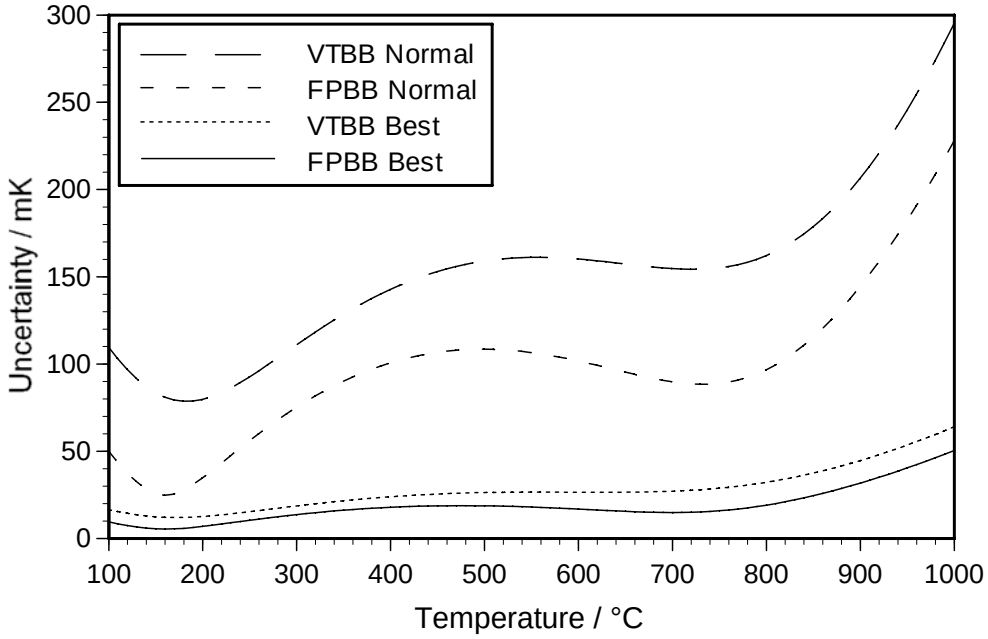

Figure 1. Total uncertainty (excluding drift) for a 1.6 μm thermometer using three calibration points. For the FPBB scheme the calibration points are the In, Al, and Ag points, and for the VTBB scheme they are 150 °C, 550 °C, and 960 °C.

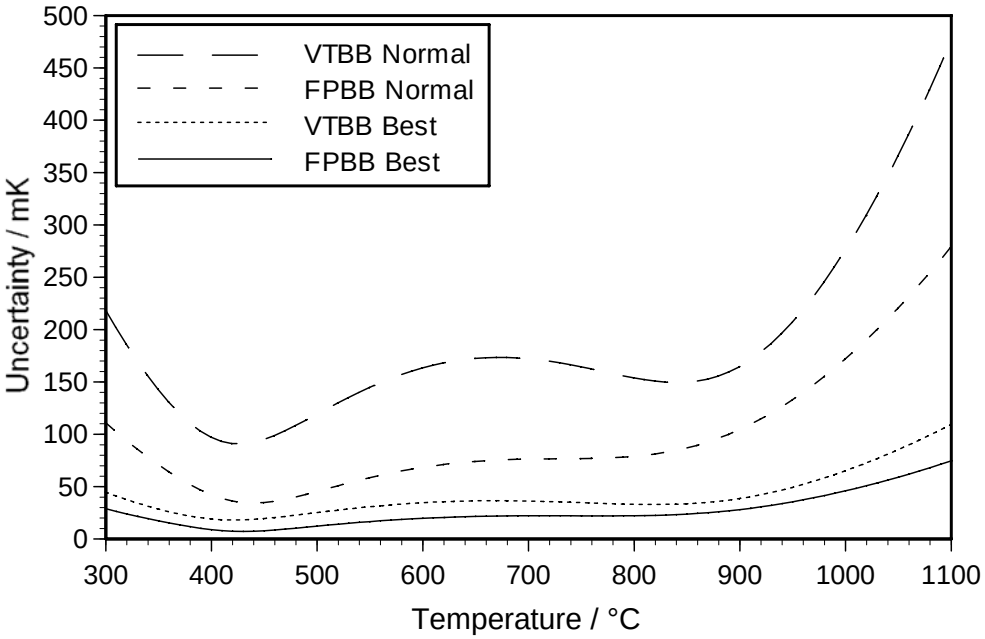

Figure 2. Total uncertainty (excluding drift) for a 0.9 μm thermometer using three calibration points. For the FPBB scheme the calibration points are the Zn, Al, and Ag points, and for the VTBB scheme they are 400 °C, 700 °C, and 960 °C.

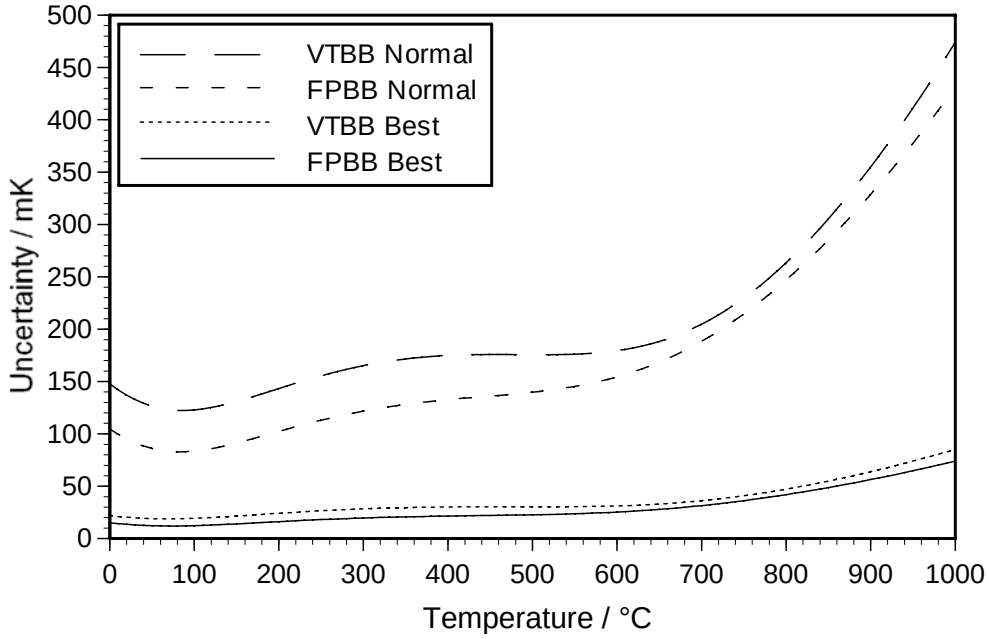

Figure 3. Total uncertainty (excluding drift) for a 3.9 μm thermometer using three calibration points. For the FPBB scheme the calibration points are the Ga, Zn and Ag points, and for the VTBB scheme they are 20 °C, 470 °C, and 960 °C.

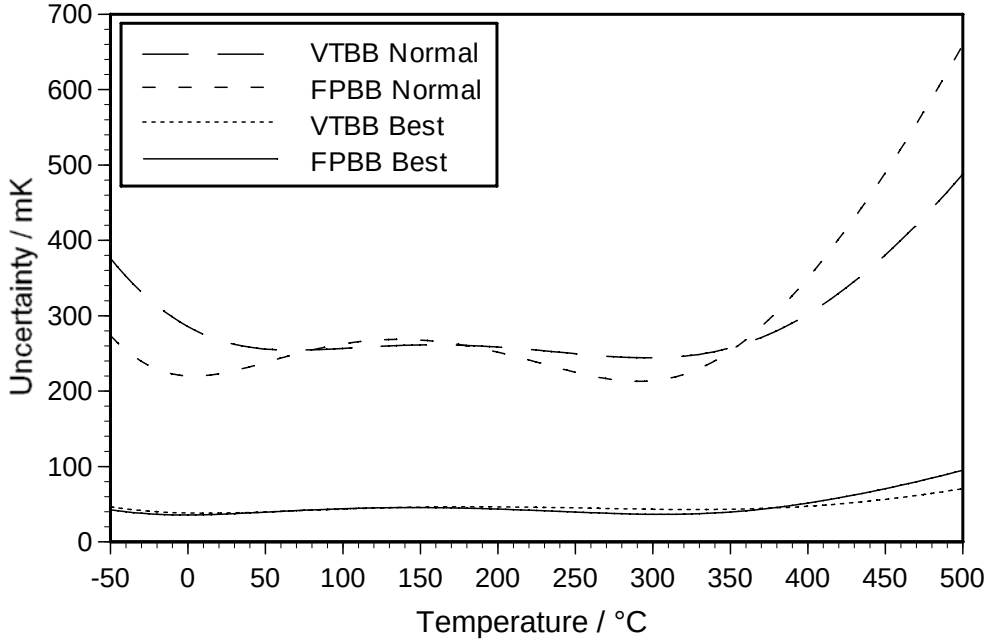

Figure 4. Total uncertainty (excluding drift) for an 8 μm to 14 μm thermometer using three calibration points. For the FPBB scheme the calibration points are the Hg, Sn and Zn points, and for the VTBB scheme they are –40 °C, 230 °C, and 500 °C.

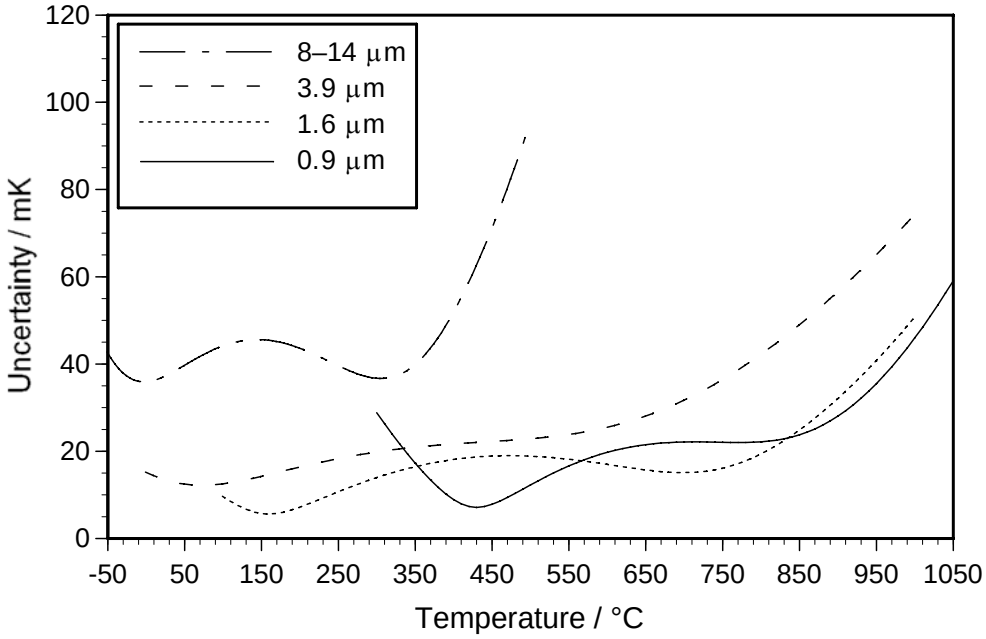

Figure 5. Comparison of the total uncertainties (excluding drift) for each thermometer for the three-point FPBB scheme at best accuracy.

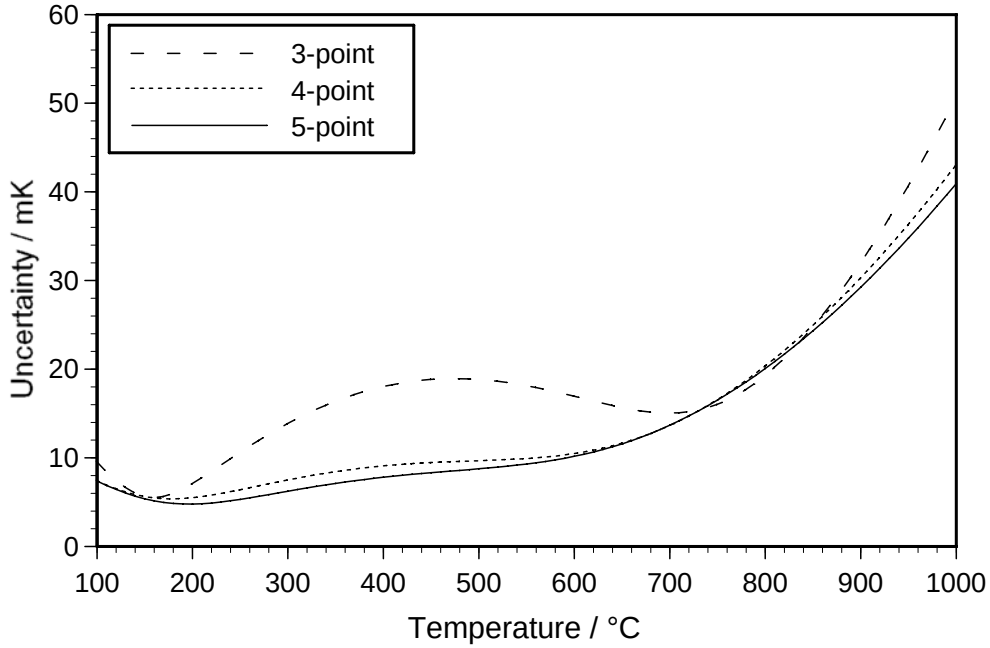

Figure 6. Comparison of uncertainty for the FPBB scheme for a 1.6 μm thermometer between 3-point interpolation and 4-point and 5-point least-squares fitting for best accuracy. The fixed points are: In, Al, Ag (3-point); In, Zn, Al, Ag (4-point); In, Sn, Zn, Al, Ag (5-point).

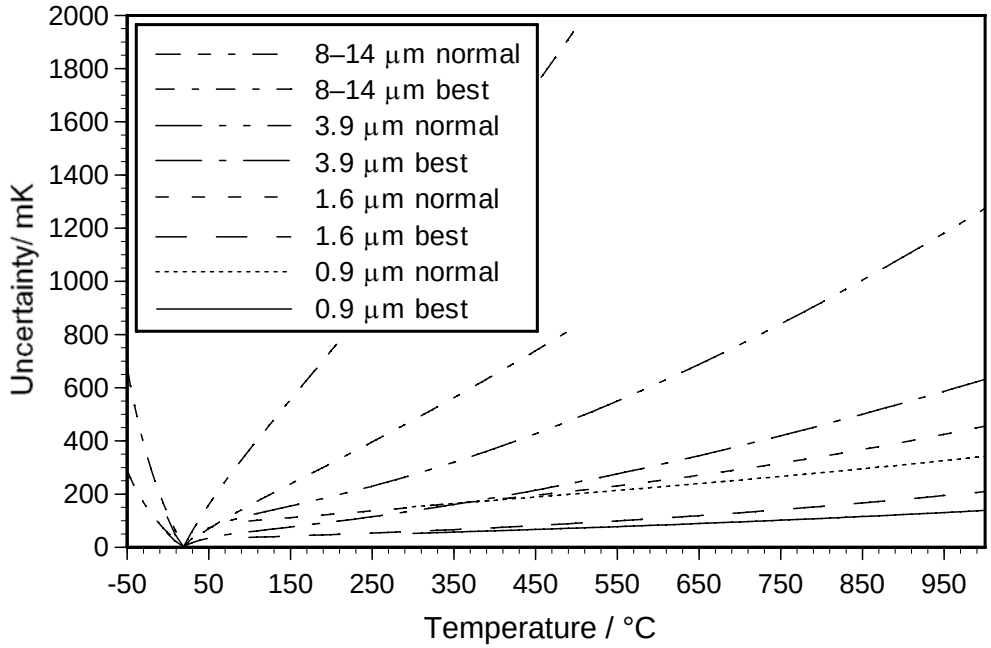

Figure 7. Drift component of uncertainty over one year.

Appendix – Inclusion of the In-Use Non-Linearity Uncertainty Component

Assume the non-linearity function for a radiation thermometer can be written as a function of signal in terms of n parameters, b_1, b_2, …, b_n:

$$\eta = \eta(S; b_1, b_2, ..., b_n) = \eta(S; \eta_1, \eta_2, ..., \eta_M) \,, \tag{A1}$$

where η describes the relative non-linearity, $\Delta S/S$, and η_1, η_2, …, η_M are M measurements of the relative non-linearity [47]. The parameters b_1, b_2, …, b_n are determined by exact or least-squares fitting of the non-linearity function to the measured values. The propagation of error formula for equation (A1) is obtained by differentiation with respect to each of the measured non-linearity values. This can be written [7]:

$$d\eta(S) = \sum_{j=1}^{M} d\eta_j \; g_j(S) \,, \tag{A2}$$

where the $g_j(S)$ functions are the sensitivity coefficients and are given by the analogue of equation (47) applied to equation (A1) for exact fitting ($M = n$) and by the analogue of equation (53) for least-squares fitting ($M > n$).

The error in the measured temperature due to the relative non-linearity error of equation (A1) is obtained by propagating the errors at the calibration points together with that at the unknown temperature. This is given by

$$dT = \left(dS - \sum_{i=1}^{N} \frac{\partial S}{\partial S_i} dS_i \right) \Bigg/ \left(\frac{\partial S}{\partial T} \right), \tag{A3}$$

where dS_i/S_i are the relative non-linearity errors, $d\eta(S_i)$, at each of the N calibration points, dS/S is the relative non-linearity error at the unknown temperature, and $\partial S/\partial S_i$ are the sensitivity coefficients given by equation (47) or (53). When there are three calibration points ($N = 3$), and in the Wien approximation, equation (A3) becomes

$$\begin{aligned} dT &= \frac{\lambda_T T^2}{c_2} \sum_{j=1}^{M} d\eta_j g_j(S) - \sum_{i=1}^{3} \frac{\lambda_{T_i} T_i^2}{c_2} L_i(T) \sum_{j=1}^{M} d\eta_j g_j(S_i) \\ &= \sum_{j=1}^{M} d\eta_j \left[\frac{\lambda_T T^2}{c_2} g_j(S) - \sum_{i=1}^{3} \frac{\lambda_{T_i} T_i^2}{c_2} L_i(T) g_j(S_i) \right], \end{aligned} \tag{A4}$$

Thus, the propagation of uncertainty formula for non-linearity, including both calibration and in-use terms, becomes

$$u_{\mathrm{NL}}^2(T) = \sum_{j=1}^{M} u^2(\eta_j) \left[\frac{\lambda_T T^2}{c_2} g_j(S) - \sum_{i=1}^{3} \frac{\lambda_{T_i} T_i^2}{c_2} L_i(T) g_j(S_i) \right]^2 , \tag{A5}$$

where $u(\eta_j)$ are the uncertainties in each of the measurements of relative non-linearity. The factors in squares brackets are the sensitivity coefficients of $u(\eta_j)$, each of which can be recognised as an interpolation error of the function $\lambda_T T^2 g_j(S)/c_2$ when fitted with a quadratic polynomial [63]. This has zeros at each of the three calibration points. For least-squares fitting, this interpolation error still contains three zeros, but they occur at points away from the calibration points. Relaxing the Wien approximation involves the same replacements in equations (A4) and (A5) as mentioned in the paragraph containing expression (51).

The non-linearity component in Figures 1 to 6 has been determined assuming a non-linearity function of the form [64]

$$\eta(S) = b_1 + b_2 S^{1/2} \,. \tag{A6}$$

In order to simplify the calculation, it has also been assumed that the b_1 and b_2 coefficients have been determined from $M = 2$ measurements of non-linearity, the first at a signal level corresponding to the lowest calibration point and the second at that of the highest calibration point. Each of these non-linearity measurements is assumed to have a relative uncertainty given by the $u_{12}(S_i)/S_i$ values in Table 15. Under these assumptions, the $g_j(S)$ functions in equation (A5) can be written without explicit reference to b_1 and b_2 as:

$$g_1(S) = \frac{S^{1/2} - S_2^{1/2}}{S_1^{1/2} - S_2^{1/2}}, \quad g_2(S) = \frac{S^{1/2} - S_1^{1/2}}{S_2^{1/2} - S_1^{1/2}} \,. \tag{A7}$$

References

[1] J Fischer, M Battuello, M Sadli, M Ballico, S N Park, P Saunders, Z Yuan, B C Johnson, E van der Ham, W Li, F Sakuma, G Machin, N Fox, S Ugur, M Matveyev, "Uncertainty budgets for realisation of scales by radiation thermometry", CCT document CCT/03-03, 2003.

[2] *Guide to the Expression of Uncertainty in Measurement*, Geneva, International Organization for Standardization, 1993.

[3] F Sakuma, S Hattori, "Establishing a practical temperature standard by using a narrow-band radiation thermometer with a silicon detector", in *Temperature: Its Measurement and Control in Science and Industry*, vol. 5, edited by J F Schooley, New York, AIP, 421–427, 1982.

[4] P Saunders, "General interpolation equations for the calibration of radiation thermometers", *Metrologia*, **34**, 201–210, 1997.

[5] F Sakuma, M Kobayashi, "Interpolation equations of scales of radiation thermometers", in *Proceedings of TEMPMEKO '96, Sixth International Symposium on Temperature and Thermal Measurements in Industry and Science*, edited by P Marcarino, Levrotto & Bella, Torino, 305–310, 1997.

[6] B Gutschwager, J Fischer, "An InGaAs radiation thermometer with an accurate reference function as transfer standard from 150 °C to 960 °C", in *Proceedings of TEMPMEKO '99, Seventh International Symposium on Temperature and Thermal Measurements in Industry and Science*, edited by J F Dubbeldam, M J de Groot, IMEKO/NMi Van Swinden Laboratorium, Delft, 567–572, 1999.

[7] P Saunders, "Propagation of uncertainty for non-linear calibration equations with an application in radiation thermometry", *Metrologia*, **40**, 93–101, 2003.

[8] E Renaot, G Bonnier, "Combined standard uncertainty — SPRT calibration at the water triple point", CCT document CCT/2000-16, 2000.

[9] E Renaot, G Bonnier, "Combined standard uncertainty — SPRT calibration according to ITS-90", CCT document CCT/2000-17, 2000.

[10] B Fellmuth, J Fischer, E Tegeler, "Uncertainty budgets for characteristics of SPRTs calibrated according to the ITS-90", CCT document CCT/01-02, 2001.

[11] J Wu, Z Yuan, Y Duan, T Wang, Q Zhao, "The realization of zinc fixed-point by radiation thermometry at NIM", in *Proceedings of TEMPMEKO 2001, 8th International Symposium on Temperature and Thermal Measurements in Industry and Science*, edited by B Fellmuth, J Seidel, G Scholz, VDE Veerlag GmbH, Berlin, 189–194, 2002.

[12] J Ancsin, "Impurity dependence of the aluminium point", *Metrologia*, **40**, 36–41, 2003.

[13] G Bongiovanni, L Crovini, P Marcarino, "Effects of dissolved oxygen and freezing techniques on the silver freezing point", *Metrologia*, **11**, 125–132, 1975.

[14] T Ricolfi, F Lanza, *High Temp.–High Press.*, "The silver and copper freezing points as accurate reference standards for radiation pyrometry", **9**, 483–487, 1977.

[15] J Fischer , H J Jung, "Determination of the thermodynamic temperatures of the freezing points of silver and gold by near-infrared pyrometry", *Metrologia*, **26**, 245–252, 1989.

[16] B W Mangum, P Bloembergen, B Fellmuth, P Marcarino, A I Pokhodun, "On the influence of impurities on fixed-point temperatures", CCT document CCT/99-11, 1999.

[17] D Ripple, B Fellmuth, M de Groot, Y Hermier, K D Hill, P P M Steur, A Pokhodun, M Matveyev, P. Bloembergen, "Methodologies for the estimation of uncertainties and the correction of fixed-point temperatures attributable to the influence of chemical impurities", CCT WG1 report, CCT document CCT/05-08, 2005.

[18] H Okamoto, *Desk Handbook: Phase Diagrams for Binary Alloys*, ASM International, p. 14, 2000.

[19] L Ma, F Sakuma, "Long term stability of silver- and aluminum-point blackbodies", in *Proceedings of SICE 2004 Annual Conference*, pp 323–328, 2004.

[20] R E Bedford, in *Theory and Practice of Radiation Thermometry*, edited by DeWitt and Nutter, John Wiley and Sons, New York, 1988.

[21] V I Sapritsky and A V Prokhorov, "Calculation of the Effective Emissivities of Specular-Diffuse Cavities by the Monte Carlo Method", *Metrologia,* **29,** 9–14, 1992.

[22] J Ishii, M Kobayashi, F Sakuma, "Effective emissivities of black-body cavities with grooved cylinders", *Metrologia*, **35**, 175–180, 1998.

[23] Y Shimizu, J Ishii, F Sakuma, A Ono, "Development of an infrared radiation thermometer and a large-opening zinc-point blackbody for the middle temperature standards", *Proceedings of TEMPMEKO 2004, 9th International Symposium on Temperature and Thermal Measurements in Industry and Science,* D Zvizdic (ed.), Zagreb; LPM FSB, ISBN 953-6313-72-3, 509–514, 2005.

[24] T P Jones, "A NML (Australia) facility for the calibration of radiation pyrometers from 50 °C to 2000 °C", In *Temperature: Its Measurement and Control in Science and Industry*, vol. 6, edited by J F Schooley, American Institute of Physics, New York, 1105–1110, 1992.

[25] M Ballico, "Modelling the effective emissivity of a graphite tube blackbody", *Metrologia*, **32**, 259–265, 1995/6.

[26] E van der Ham et al., "TRIRAT: Traceability in infrared radiation thermometry from –50 °C to 800 °C", a framework 4 project of the Standards, Measurement and Testing programme of the European Commission, contract no SMT 4-CT-96-2060.

[27] M Ballico, "A simple technique for measuring the infrared emissivity of blackbody radiators", *Metrologia*, **37**, 295–300, 2000.

[28] M Ballico, "The CSIRO-NML radiation thermometry calibration facility", *Proceedings of TEMPMEKO 2004, 9th International Symposium on Temperature and Thermal Measurements in Industry and Science,* D Zvizdic (ed.), Zagreb; LPM FSB, ISBN 953-6313-72-3, 841–846, 2005.

[29] S Mekhontsev, V Khromchenko, A Prokhorov, L Hanssen, "Emissivity evaluation of fixed point blackbodies", *Proceedings of TEMPMEKO 2004, 9th International Symposium on Temperature and Thermal Measurements in Industry and Science,* D Zvizdic (ed.), Zagreb; LPM FSB, ISBN 953-6313-72-3, 581–586, 2005.

[30] M Ballico, private communication.

[31] J Hartmann, D Taubert, J Fischer., "Characterization of the double-heatpipe blackbody LABB for use at temperatures below 500 °C", in *Proceedings of TEMPMEKO '99, Seventh International Symposium on Temperature and Thermal Measurements in Industry and Science*, edited by J F Dubbeldam, M J de Groot, IMEKO/NMi Van Swinden Laboratorium, Delft, 511–516, 1999.

[32] P Bloembergen, Y Yamada, N Yamamoto, J Hartmann, "Realizing the high-temperature part of a future ITS with the aid of eutectic metal-carbon fixed points", in *Temperature: Its Measurement and Control in Science and Industry*, Vol. 7, edited by D C Ripple et al., AIP Conference Proceedings, Melville, New York, 291-296, 2003.

[33] J Hartmann, S Schiller, R Friedrich, J Fischer, "Non-isothermal temperature distribution and resulting emissivity corrections for the high temperature blackbody BB3200", in *Proceedings of TEMPMEKO 2001, 8th International Symposium on Temperature and Thermal Measurements in Industry and Science*, edited by B Fellmuth, J Seidel, G Scholz, VDE Verlag GmbH, Berlin, 227–232, 2002.

[34] S Hattori, A Ono, "The effective temperature to express radiant characteristics of nonisothermal cavities", in *Temperature: Its Measurement and Control in Science and Industry*, vol. 5, edited by J F Schooley, New York, AIP, 521–727, 1982.

[35] H J Jung, "Determination of the difference between the thermodynamic fixed-point temperatures of gold and silver by radiation thermometry", *Inst. Phys. Conf.*, Ser. No. 26, 278–286, 1975.

[36] P Jimeno-Largo, Y Yamada, P Bloembergen, M A Villamanan, G Machin, "Numerical analysis of the temperature drop across the cavity bottom of high-temperature fixed points for radiation thermometry", *Proceedings of TEMPMEKO 2004, 9th International Symposium on Temperature and Thermal Measurements in Industry and Science,* D Zvizdic (ed.), Zagreb; LPM FSB, ISBN 953-6313-72-3, 335–340, 2005.

[37] H McEvoy, G Machin, "Report on the thermal conductivity of graphite", produced for CCT WG5, 11 pp, 2001.

[38] J Fischer, "Developments in infrared radiation thermometry", in *Proceedings of TEMPMEKO '99, Seventh International Symposium on Temperature and Thermal Measurements in Industry and Science*, edited by J F Dubbeldam, M J de Groot, IMEKO/NMi Van Swinden Laboratorium, Delft, 27–34, 1999.

[39] J Ishii, A Ono, "Low-temperature infrared radiation thermometry at NMIJ", in *Temperature: Its Measurement and Control in Science and Industry*, Vol. 7, edited by D C Ripple et al., AIP Conference Proceedings, Melville, New York, 657-662, 2003.

[40] M Ballico, "High precision measurement of the emissivity of small fixed point blackbodies", in *Proceedings of TEMPMEKO 2001, 8th International Symposium on Temperature and Thermal Measurements in Industry and Science*, edited by B Fellmuth, J Seidel, G Scholz, VDE Verlag GmbH, Berlin, 233–237, 2002.

[41] D Lowe, M Battuello, G Machin, F Girard, "A comparison of size of source effect measurements of radiation thermometers between IMGC and NPL", in *Temperature: Its Measurement and Control in Science and Industry*, Vol. 7, edited by D C Ripple et al., AIP Conference Proceedings, Melville, New York, 625–630, 2003.

[42] G Machin, R Sergienko, "A comparative study of size of source effect (SSE) determination techniques", in *Proceedings of TEMPMEKO 2001, 8th International Symposium on Temperature and Thermal Measurements in Industry and Science*, edited by B Fellmuth, J Seidel, G Scholz, VDE Veerlag GmbH, Berlin, 155–160, 2002.

[43] P Bloembergen, Y Duan, R Bosma, Z Yuan, "The characterization of radiation thermometers subject to the size-of-source effect", in *Proceedings of TEMPMEKO '96, Sixth International Symposium on Temperature and Thermal Measurements in Industry and Science*, edited by P Marcarino, Levrotto & Bella, Torino, 261–266, 1997.

[44] H W Yoon, D W Allen, R D Saunders, "Methods to reduce the size-of-source effect in radiometers", *Metrologia*, **42**, 89–96, 2005.

[45] T Ricolfi, F Girard, "A transfer standard infrared thermometer for the temperature range 150 °C to 1000 °C", in *Proceedings of TEMPMEKO '99, Seventh International Symposium on Temperature and Thermal Measurements in Industry and Science*, edited by J F Dubbeldam, M J de Groot, IMEKO/NMi Van Swinden Laboratorium, Delft, 593–598, 1999.

[46] P Bloembergen, "On the correction for the size-of-source effect corrupted by background radiation", in *Proceedings of TEMPMEKO '99, Seventh International Symposium on Temperature and Thermal Measurements in Industry and Science*, edited by J F Dubbeldam, M J de Groot, IMEKO/NMi Van Swinden Laboratorium, 607–612, 1999.

[47] P Saunders, D R White, "Propagation of uncertainty due to non-linearity in radiation thermometers", *Int. J. Thermophys*., **28**, 2098–2110, 2007.
[48] L P Boivin, "Automated absolute and relative spectral linearity measurements on photovoltaic detectors", *Metrologia*, **30**, 355–360, 1993.
[49] R D Saunders, J B Shumaker, "Automated radiometric linearity tester", *Applied Optics*, **23**, 1984.
[50] L P Boivin, "Properties of sphere radiometers suitable for high-accuracy cryogenic-radiometer-based calibrations in the near-infrared", *Metrologia*, **37**, 273–278, 2000.
[51] P Corredera, M L Hernanz, M González-Herráez, J Campos, "Anomalous non-linear behaviour of InGaAs photodiodes with overfilled illumination", *Metrologia*, **40**, S150–S153, 2003.
[52] H W Yoon, J J Butler, T C Larason, G P Eppeldauer, "Linearity of InGaAs photodiodes", *Metrologia*, **40**, S154–S158, 2003.
[53] M Battuello, P Bloembergen, F Girard, T Ricolfi, "A comparison of two methods for measuring the nonlinearity of infrared radiation thermometers", in *Temperature: Its Measurement and Control in Science and Industry*, Vol. 7, edited by D C Ripple et al., AIP Conference Proceedings, Melville, New York, 613–618, 2003.
[54] L P Boivin, "Properties of indium antimonide detectors for use as transfer standards for detector calibrations", *Applied Optics*, **37**, 1924–1929, 1998.
[55] E Theocharous, J Ishii, N P Fox, "Absolute linearity measurements on HgCdTe detectors in the infrared region", *Applied Optics*, **43**, 4182–4188, 2004.
[56] J Ishii, M Kobayashi, F Sakuma, A Ono, "DC-operated InSb radiation thermometer for precision measurement near room temperatures", in *Proceedings of TEMPMEKO '99, Seventh International Symposium on Temperature and Thermal Measurements in Industry and Science*, edited by J F Dubbeldam, M J de Groot, IMEKO/NMi Van Swinden Laboratorium, Delft, 625-630, 1999.
[57] O Struβ, "Transfer radiation thermometer covering the temperature range from –50 °C to 1000 °C", in *Temperature: Its Measurement and Control in Science and Industry*, Vol. 7, edited by D C Ripple et al., AIP Conference Proceedings, Melville, New York, 565–570, 2003.
[58] K Chrzanowski, "Experimental verification of a theory of the influence of measurement conditions on temperature measurement accuracy with IR systems", *Applied Optics*, **35**, 3540–3547, 1996.
[59] D G Crowe, P R Norton, T Limperis, J Mudar, Chapter 4 "Detectors", in *The Infrared and Electro-Optical Systems Handbook*, Volume 3, "Electro-Optical Components", edited by W D Rogatto, SPIE Optical Engineering Press, Bellingham, Washington, 1993.
[60] P Saunders, D R White, "Interpolation errors for radiation thermometry", *Metrologia*, **41**, 41–46, 2004.
[61] S-G Park, B-K Kim, C-W Park, D-H Lee, "Realization of radiance temperature scale from 500 K to 1,250 K by a radiation thermometer with a thermal detector", *International Journal of Thermophysics*, **29**, 301–311, 2008.
[62] P Saunders, D R White, "Physical basis of interpolation equations for radiation thermometry", *Metrologia*, **40**, 195–203, 2003.
[63] D R White, P Saunders, "The propagation of uncertainty on interpolated scales, with examples from thermometry", *Metrologia*, **37**, 285–293, 2000.
[64] H J Jung, "Spectral nonlinearity characteristics of low noise silicon detectors and the application to accurate measurements of radiant flux ratios", *Metrologia*, **15**, 173–181, 1979.